12-2023

Experimental Investigation of Low Thermal Inertia Thermal Barrier Coatings for Spark Ignition Engines

John Gandolfo
gandolf@clemson.edu

Recommended Citation

Gandolfo, John, "Experimental Investigation of Low Thermal Inertia Thermal Barrier Coatings for Spark Ignition Engines" (2023). *All Theses*. 4202.
https://tigerprints.clemson.edu/all_theses/4202

EXPERIMENTAL INVESTIGATION OF LOW THERMAL INERTIA THERMAL BARRIER COATINGS FOR SPARK IGNITION ENGINES

A Thesis
Presented to
the Graduate School of
Clemson University

In Partial Fulfillment
of the Requirements for the Degree
Master of Science
Automotive Engineering

---

by
John Gandolfo
December 2023

Accepted by:
Dr. Benjamin Lawler, Committee Chair
Dr. Zoran Filipi
Dr. Brian Gainey

ABSTRACT

The application of thermal barrier coatings (TBCs) in spark ignition (SI) engines has historically been avoided due to the knock penalty associated with higher surface temperatures induced by the ceramic layer. However, advances in low thermal inertia coatings (i.e., temperature swing coatings) that combine low thermal conductivity with low volumetric heat capacity can prevent excessively high surface temperatures during the intake stroke and reduce or avoid knock while improving performance and efficiency. This thesis experimentally evaluates the effectiveness of these low thermal inertia coatings in a single-cylinder research engine representative of modern SI engines.

First, four pistons coated with a novel, low thermal inertia material (called NC) and one piston coated with commercially available gadolinium zirconate (GZO) were tested. An average 0.15 percentage point absolute thermal efficiency gain was observed with the thinnest NC coating. This efficiency increase was enabled through spark advance, indicating that the piston surface temperature was lower than the metal reference surface temperature early in the cycle (i.e., during the intake stroke). Thicker NC coatings experienced a degradation in performance and efficiency due to charge heating increasing the knock propensity. Simulated cold-start tests demonstrated that the charge heating behavior observed with thicker coatings was beneficial for reducing unburned hydrocarbons and particulate matter emissions.

Once the best performing piston was identified, intake and exhaust valves with GZO coated combustion faces, backsides, and stems were installed to evaluate the effect of additional coated surface area on performance. With both coated valves and a coated piston, the net thermal efficiency increased by 0.20 percentage points, thus the valves contributed an average of 0.05

percentage points over the coated piston. A staged valve removal was performed to determine the contribution of each coated valve. It was found that the coated exhaust valve promoted knock and higher exhaust temperature, whereas the coated intake valve encountered lower knock propensity as heat transfer between the valve and incoming air was reduced.

Finally, a pseudo-durability test was performed to analyze the effect of naturally grown thermal TBCs (i.e., combustion chamber deposits – CCDs) on low thermal inertia TBCs. A coated piston and coated heat flux probe underwent a low-load operating condition for 62.5-hours to promote CCD growth. Every 12.5-hours, the performance at a knock limited condition was assessed and thermophysical property measurements on the heat flux probe were performed. Net thermal efficiency increased by 0.4 percentage points after 12.5-hours, but further CCD growth caused a dithering of efficiency between 12.5-hours and the baseline condition. The knock limited spark advance was consistently retarded throughout this period. External property measurements with the coated heat flux probe showed an improvement in the thermophysical properties of the TBC/CCD layer.

ACKNOWLEDGMENTS

This work was funded by the Department of Energy Small Business Innovation Research (DOE-SBIR) Program Award No. DE-SC0019865, titled *Novel Thermal Barrier Coatings for Gasoline Spark Ignition Engines*. All coated components in this study were produced by Solution Spray Technologies. Additional funding was provided by Ford Motor Company through their University Research Program.

TABLE OF CONTENTS

LIST OF TABLES

LIST OF FIGURES

LIST OF ABBREVIATIONS

aTDC	after Top Dead Center
APS	Air Plasma Spray
BEV	Battery electric vehicle
CAD	Crank Angle Degree
CA50	crank angle of 50% mass fraction burned
CCDs	Combustion Chamber Deposits
CO	Carbon Monoxide
DI	Direct Injection
EVO	Exhaust Valve Opening
GZO	Gadolinium Zirconate
HCCI	Homogeneous Charge Compression Ignition
ICE	Internal combustion engine
$IMEP_n$	Net Indicated Mean Effective Pressure
IVO	Intake Valve Opening
KLSA	Knock Limited Spark Advance
MBT	Maximum Brake Torque
NC	Novel Low Thermal Inertia Coating
PFI	Port-Fuel Injection
PM	Particulate Matter
SI	Spark Ignition
TBCs	Thermal Barrier Coatings
uHC	Unburned Hydrocarbon
YSZ	Yttria Stabilized Zirconia

CHAPTER 1. INTRODUCTION

1.1 Overview of TBCs in Internal Combustion Engines

Increasing concerns over the effects of global climate change have driven the world governments and organizations to reduce the output of greenhouse gas emissions. The road transportation sector contributes approximately 15% of global CO_2 emissions [1]. This has generated significant interest in electrifying passenger vehicles to eliminate tailpipe emissions. However, several challenges and obstacles have persisted with this energy approach. Even though the battery electric vehicle (BEV) itself produces no greenhouse gas emissions, the electricity required to charge the vehicle may be generated through a variety of sources such as fossil fuels (oil, natural gas, coal, etc.) or renewable sources (hydroelectric, geothermal, etc.), thus shifting the emissions burden from the vehicle to the power station [2]. Further analysis of the regional breakdown in the energy used to generate electricity across the United States shows wide state-by-state variety, illustrating a complicated picture on the true-zero emission potential of BEVs [3]. When compounded with the high CO_2 penalty associated with material extraction and battery production [4], life cycle assessments have produced mixed results regarding the environmental impact of BEVs compared to internal combustion engine (ICE) powered vehicles [5], [6], [7], [8], [9].

Even though electric vehicles will be important for achieving future transportation and climate goals, the ICE will remain crucial for the transportation industry. This makes small, incremental improvements still worthy of pursuit. Improvements in thermal management with the intent of reducing heat transfer losses out of the cylinder have been the subject of research for several decades. From a thermodynamic perspective, heat transfer losses constitute up to 25% of the fuel energy input, thus any reduction in of those losses can increase system efficiency [10].

Though they were originally intended for gas turbine applications, researchers have identified thermal barrier coatings (TBCs) as the appropriate technology to achieve this goal. The TACOM/Cummings Adiabatic Engine program was the first major attempt to implement TBCs within the ICE architecture. Even though a truly adiabatic engine was a thermodynamically ambitious goal, the project successfully demonstrated that TBCs can enable significant enough heat transfer reductions such that the forced coolant system could be removed [11].

The reduction in heat transfer losses through elevated surface temperatures from TBCs introduced a charge heating effect. The calculated cylinder wall temperature of various coating thicknesses in the Adiabatic Engine Program was significantly higher throughout the entire engine cycle compared to the uninsulated surfaces, with thicker coatings maintaining higher surface temperatures [11]. Although increasing the coating thickness could further reduce heat transfer losses, higher surface temperatures heated the incoming air, reduced charge density, and decreased the volumetric efficiency. Additionally, the elevated surface temperature changes the thermal environment of the cylinder and the auto-ignition tendency of the fuel. In a gasoline fueled spark-ignition (SI) engine, the research community has generally avoided TBC application due to these factors. SI engines are knock-limited with low compression ratios and retarded combustion phasing at high loads. Knock is highly sensitive to in-cylinder temperatures [12], thus an increase in temperature from charge heating will increase the propensity for end-gas knock, potentially damaging the engine and the coating. To compensate for any induced knock from the TBC, the spark timing would have to be retarded, potentially surrendering the efficiency increase associated with blocked heat transfer.

Due to the knock constraint, research on TBCs in SI is quite limited, but generally point to thin coatings when a notable difference in performance between coated and uncoated configurations was encountered. Wong et al. created a model to fundamentally study the effect of thin ceramic coatings on combustion performance [13]. The authors first studied how thermal efficiency changed with heat transfer by varying the wall temperature from 500 K, 700 K, and 900 K during each stroke of the cycle. Increasing the intake stroke wall temperature did not significantly change the amount of heat transfer blocked and thermal efficiency deteriorated by ~0.8 percentage points. Increasing the wall temperature during the compression and expansion stroke (with constant intake wall temperature) showed an increase in thermal efficiency by ~0.8 percentage points. This parametric study demonstrated that elevated surface temperatures are not uniformly beneficial across all engine strokes. The authors then introduced various coatings with different thermophysical properties and showed that the increase in thermal efficiency diminishes and levels off after a certain thickness. Assanis and Mathur investigated thin plasma sprayed coatings (less than 270-microns) on the cylinder head, valves, ports, piston, and liner of a 4-cylinder spark ignition engine [14]. Across all operating conditions, the authors reported no significant knock penalty. Part load operating conditions experienced notable reductions in brake specific fuel consumption over the uncoated configuration, but performance at wide open throttle was generally equal between coated and uncoated cases. Direct heat flux measurements of a metal-based TBC showed no significant reduction in heat transfer compared to a baseline piston [15]. Measurements in a follow up study with an yttria stabilized zirconia coating showed no statistically significant change in average heat flux [16]. Poola et al. used a 500-micron partially stabilized zirconia coating on the cylinder head and piston of a two-stroke SI engine fueled with gasoline and methanol [17]. Broad brake thermal efficiency improvements were recorded across multiple speeds under part load conditions, but operating with gasoline at high loads presented a loss in brake power and frequent knock due to charge heating. However, this detriment was advantageous for methanol as the high latent heat of vaporization absorbed heat away from the walls, resulting in charge cooling. When compounded with the high auto-ignition resistance of methanol compared to gasoline, the ceramic coated engine fueled with methanol experienced no knock across all tested operating conditions. Overall, the literature suggests that thin TBCs in SI engines have the potential to increase in-cylinder efficiency but knock induced from charge heating is the primary obstacle to successful application.

To prevent charge heating, low thermal inertia coatings (i.e., temperature swing coatings), have been proposed. Thermal inertia quantifies a material's ability to exchange heat with its surroundings, and is represented as:

$$\varepsilon = \sqrt{k\rho C_p} \tag{1}$$

where k is the thermal conductivity, ρ is the density, and C_p is the specific heat of the TBC material. Low thermal inertia coatings retain the low thermal conductivity necessary to block heat transfer with low volumetric heat capacity (ρC_p) to prevent excess heat storage in the coating during the intake stroke. Yan et al. used a 0D thermodynamic model coupled with a 1D surface temperature solver to study the impacts of varying coating thermophysical properties and thickness on performance in homogeneous charge compression ignition (HCCI) [20]. HCCI is a kinetically driven combustion process that is largely controlled by the thermodynamic state of the cylinder, thus any effect of blocked heat transfer is easily captured. Reducing thermal conductivity elevated the peak surface temperature during combustion and the intake stroke. Reducing the volumetric heat capacity decreased the surface temperature during the intake stroke, counteracting the charge heating induced from low thermal conductivity. This combination of thermophysical properties allow the surface temperature to dynamically change with gas temperature [19]. This concept is illustrated in Figure 1, which compares the surface temperature behavior of three different coating configurations: uncoated metal piston (green line), thick TBC (red line), and temperature swing TBC (purple) [20]. The thick insulation incurs a significant charge heating penalty due to its high surface temperature during the intake stroke, whereas the temperature swing insulation achieves a dynamic temperature that allows the surface temperature to drop comparably to the metal piston temperature during the intake stroke. Between the two TBCs, the temperature swing (i.e., difference between maximum and minimum surface temperature) is approximately equal during combustion, which results in approximately the same amount of heat transfer reduction without a significant volumetric efficiency penalty.

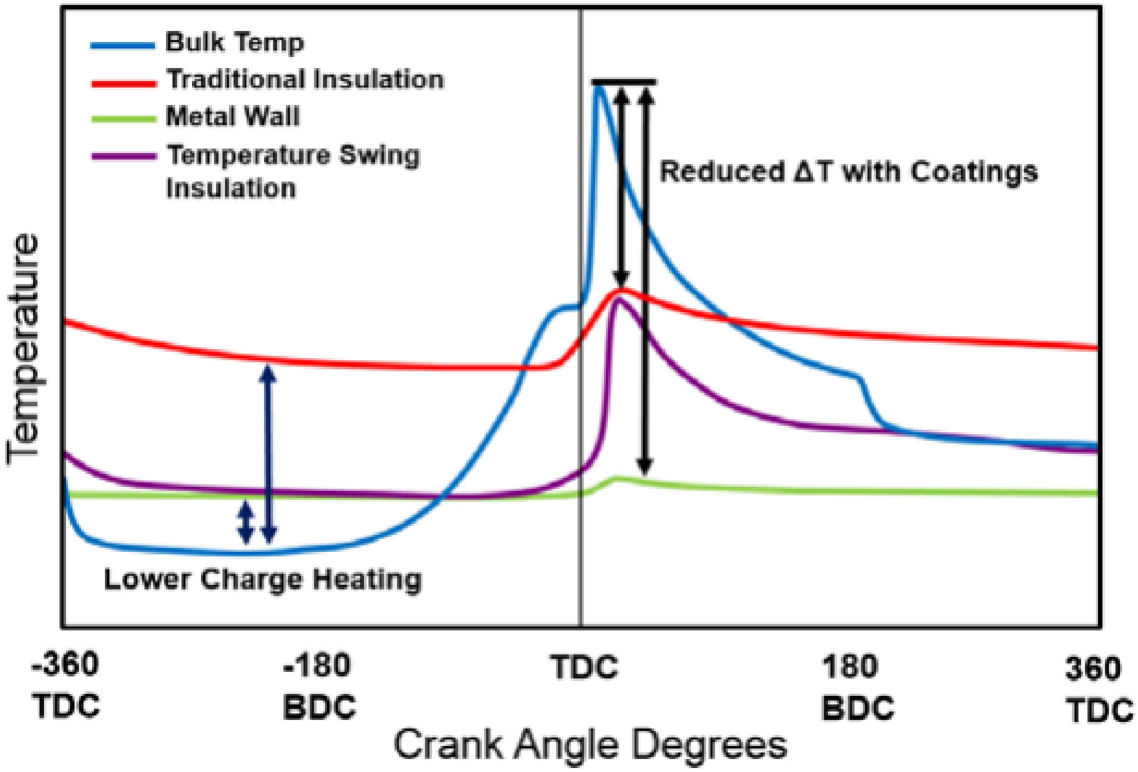

Figure 1: Surface temperatures for baseline metal piston (green line), traditional TBC (red line), and temperature swing insulation (purple line) [20].

In a premixed, kinetically controlled mode such as HCCI, experimental work has shown the viability of low thermal inertia coatings. Powell et al. tested a 150-micron yttria stabilized zirconia (YSZ) coated piston in a single-cylinder HCCI engine [21]. The authors also installed a fast response heat flux probe coated with the same material and similar thickness (157-microns) in the cylinder head to evaluate changes in heat flux on a crank-angle basis. With the fueling rate, air-fuel ratio, and temperature kept constant between the baseline and coated configurations, the authors recorded a 2.2-4.9 crank angle advancement in the heat release process, which was indicative of more favorable conditions for fuel ignition due to lower heat transfer losses. This corresponded to a ~2.5 percentage point increase in gross indicated thermal efficiency. The heat flux probes confirmed the peak heat flux out of the cylinder was lower with the coated piston and the surface temperature of the piston was able to achieve similar temperatures to that of the uncoated piston during the intake stroke, indicating that the thin coating heaved like a low thermal inertia coating and minimized charge heating. Further work with a YSZ coated piston featuring structured porosity to further enhance its thermophysical properties also demonstrated further improvement over a denser version of the coating [22].

Experiments focused on low thermal inertia coatings in SI engines are scarce and present conflicting results. Despite recording a 100°C temperature swing and no volumetric efficiency penalty, Chérel et al. saw no efficiency changes with a low thermal inertia coating applied on the piston and cylinder head relative to a reference configuration [23]. Although no specific cause was identified, the authors suggested that the higher surface temperatures increased the convective heat transfer coefficient through lower thermal boundary thickness (which was hypothesized by Woschni et al. and terms convection vive [24]), thus counteracting the reduction in temperature difference and increasing heat transfer losses. Andrie et al. tested a novel low thermal inertia coating applied on the piston and cylinder head of a spark ignition engine fueled with natural gas [25]. At equivalent spark timings, the coating generated a 1.3 percentage point increase in brake thermal efficiency over uncoated components. The authors reported a knock limit spark advance (KLSA) extension during testing.

1.2 Overview of Combustion Chamber Deposits

SI engines already feature thermal insulators in the combustion chamber in the form of combustion chamber deposits (CCDs). As opposed to manufactured coatings derived from a powder and applied through a thermal spray process, CCDs are naturally grown over the course of engine operation. In SI operation, the quenching of the flame against the walls of the combustion chamber produce a narrow region in which hydrocarbons are not completely burned, during which addition and substitutions reactions with radical species partially oxidizes the hydrocarbon species, eventually leading to condensation and polymerization of these partially burned hydrocarbons [26], [27].

The formation of CCDs is highly dependent on both fuel composition and surface temperature. Cheng evaluated CCD formation tendency with isooctane and toluene blends, showing that increased amounts of toluene increased CCD weight [28]. The addition of aromatic compounds generally tend to increase CCD growth, whereas oxygenates such as methyl tert-butyl ether have been shown to reduce CCD growth [28], [29]. Gasolines with detergent additives have also been observed to increase CCD thickness relative to gasoline with no additives [30]. Lacey et al. investigated two different fuel blends with vastly different aromatic contents [31]. The fuel with a higher fraction of aromatics achieved a higher equilibrium thickness after a shorter period of time.

Low temperature surfaces tend to accumulate thicker CCD. Cheng used a custom sampling probe to accumulate CCD on a sample coupon at different locations in the combustion chamber to evaluate the influence of surface temperature on CCD growth [32]. Surfaces with low surface temperatures typically grew thicker CCD over a longer period of time compared to hotter surfaces. A critical surface temperature of ~310°C was identified after which CCD growth was minimal.

Since CCD growth is a function of surface temperature, several operating parameters can influence CCD growth rates. High coolant temperatures tend to stunt CCD growth, whereas leaner and richer mixtures tend to promote CCD growth due to differences in chemical reactions [28]. Spark advance was found to have little influence on CCD magnitude since thermodynamic conditions of the gas are changed and not the surface temperature or chemical state. By maintaining a stoichiometric mixture, CCD growth decreased with increasing load before slightly increasing again at the highest tested load due to soot deposits. Consequently, low load/speed operation is more favorable for CCD formation, whereas high load/speed operation can remove CCD layers due to high surface temperatures [33].

As thermal insulators, the benefits and drawbacks of CCDs are analogous to manufactured TBCs. Güralp et al. showed an advanced heat release rate over a 40-hour period due to CCD growth in HCCI [34]. The CCD-driven combustion advancement in HCCI was a result of charge heating and a reduction in compression and expansion stroke heat transfer, demonstrating that CCDs have a similar impact on the HCCI combustion process as TBCs. Further analysis with heat flux probes embedded in the cylinder head showed a reduction in local heat flux. Kalghatgi et al. showed a reduction in specific fuel consumption in an SI engine with CCDs [35]. This benefit, however, was counteracted by an increased knock tendency, which is another characteristic of thermal insulation. Barnes and Stephenson found that CCDs can improve fuel consumption by an average of 5%, but under knock limited conditions can retard ignition timing and harm fuel consumption [36]. The thermophysical properties of CCDs are varied throughout the literature due to fuel composition but are generally comparable to modern TBCs. Anderson et al. used an infrared radiometer to obtain surface temperature measurements with an embedded fast response thermocouple on the inner surface of the combustion chamber wall to experimentally determine conductivity values between 0.38 and 0.8 W/m-K for CCDs generated with several fuel blends [37]. Nishiwaki and Hafnan reported conductivity and diffusivity (ratio of conductivity and volumetric heat capacity) values between 0.25 and 1.06 W/m-K and 2.3 and 7.5 x 10^{-6} m^2/s using CCD thickness and surface and backside measurements derived from a radiation pulse [38]. Hayes flashed a CCD with a heat flux pulse for 26 nanoseconds with a laser and compared the temperature rise to the analytical solution of the one-dimensional heat transfer problem, calculating diffusivities on a cylinder head between 0.593 and 2.160 x 10^{-7} m^2/s [39].

In this thesis, experiments are performed on a SI engine to determine the in-cylinder and system level implications of a novel low thermal inertia coating. First, spark timing sweeps were performed at multiple operating conditions with several pistons of varying thickness and coating materials to evaluate the impact of this novel material on efficiency, knock and emissions in a single-cylinder research engine. Simulated cold-start tests were also performed to evaluate the transient response of these coatings on exhaust temperature ramp-up and emissions characteristics. Finally, a comprehensive durability study was performed to evaluate the impact of CCD growth on a low thermal inertia coating and its implications on knock and emissions.

CHAPTER 2. EXPERIMENTAL SETUP

2.1 Engine Experimental Test Cell

Engine experiments were performed on a custom single-cylinder Ricardo Hydra block with a prototype GM pent-roof head. The spark plug and direct injector were centrally mounted. Engine geometric details can be found in Table 1. A schematic showing the engine test cell layout is provided in Figure 2.

Table 1: Engine geometry and timings

Displacement Volume [cm^3]	**550**
Compression Ratio	**9.3**
Bore [mm]	**86.0**
Stroke [mm]	**94.6**
Connecting Rod Length [mm]	**152.2**
IVC/EVO [deg aTDC]	**-130/127**

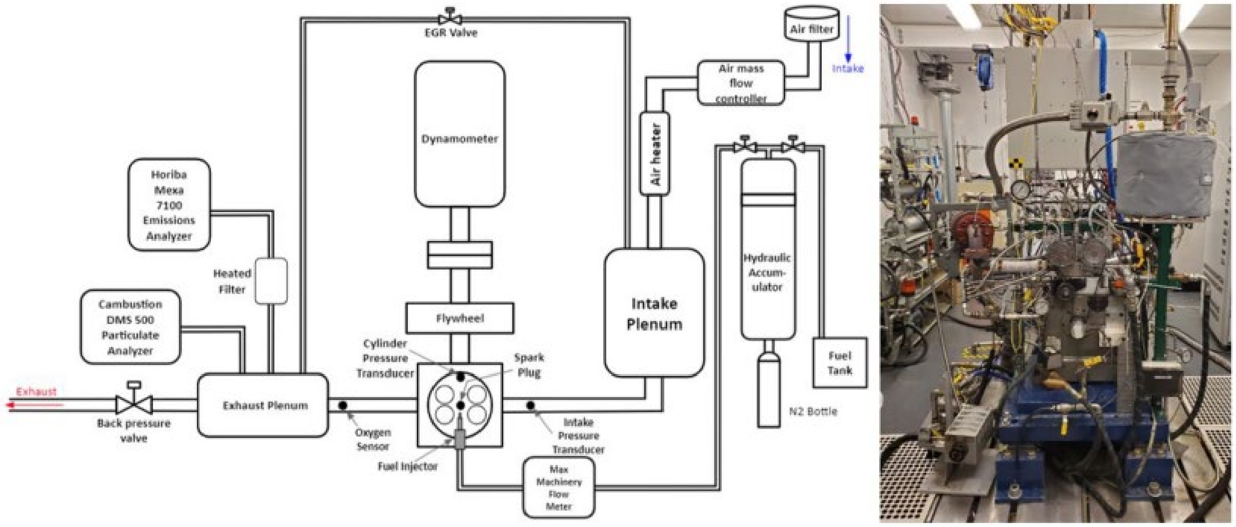

Figure 2: Engine test cell layout

Fuel flow measurements were recorded with a Max Machinery piston flow meter. Air flow was controlled and measured through an Alicat laminar flow element. Air, oil, and coolant temperatures were maintained with PID controllers. NO_x, O_2, CO, CO_2, and uHC (unburned hydrocarbons) were sampled through the exhaust plenum with a Horiba MEXA 7100 DEGR 5-gas analyzer. Intake pressure was measured with a Kistler 4007D pressure transducer. Cylinder pressure was redundantly measured with a Kistler 6115c spark plug and 6125c pressure transducers. The intake and cylinder pressures were synchronized with a Kistler crank angle encoder with 0.1 degree resolution. Additional details regarding instrumentation and uncertainty can be found in Table 2.

Table 2: Experimental instrumentation and uncertainty

Instrument	Measurement	Range	Uncertainty
Alicat MCR WH-1000	Air flow	0 – 1000 SLPM	± 0.4%
Max Machinery P213	Fuel flow	0.5 – 1800 cc/min	± 0.2%
K-type Thermocouple	Temperature	75 – 1200 K	± 0.75%
Kistler 6125c / 6115c	Cylinder Pressure	0 - 100 bar	± 0.40 / 0.50 bar
Kistler 4007D	Intake Pressure	0 - 5 bar	± 0.05 bar
Horiba MEXA 7100 $\boldsymbol{NO_x}$	NO_x	0 – 3500 ppm	± 70 ppm
Horiba MEXA 7100 $\boldsymbol{O_2}$	O_2	0 – 25% vol	± 0.5%
Horiba MEXA 7100 $\boldsymbol{CO}$	CO	0-2% vol	± 0.02%
Horiba MEXA 7100 $\boldsymbol{CO_2}$	CO_2	0-20% vol	± 0.20%
Horiba MEXA 7100 $\boldsymbol{uHC}$	uHC	0-10,000 ppm	± 100 ppm

EPA Tier III EEE certification gasoline was used in all testing. The charge was kept stoichiometric across all operating conditions with an early intake stroke injection to allow time for mixing. Fuel was pressurized to 100 bar with nitrogen through a hydraulic accumulator. A custom LabVIEW program was used to record data and control the engine. At each operating condition, 300 consecutive cycles were saved once the exhaust temperature was stabilized, indicating that steady-state operation was achieved. Data was processed in a MATLAB script that performs heat release analysis using the NASA polynomials for mixture properties [40].

Knock intensity was determined using the metric developed by Galloni in Equation (2) [41]. The individual pressure traces (j) were passed through a high pass filter to isolate the maximum absolute pressure oscillation ($P_{HPfilt,j}$). The early burn period, defined from spark crank angle (θ_{ST}) to the 50% burned mass crank angle (CA50) is compared to that of the late burn phase from 50% mass burned crank angle to exhaust valve opening crank angle (θ_{EVO}). This calculation is performed for all 300 cycles (n_{cyc}). The KLSA is defined by a knock intensity of 100%.

$$KI\ [\%]\ =\ \frac{100}{n_{cyc}}\sum_{j=1}^{n_{cyc}}\frac{max\left(P_{HPfilt,j}\Big|_{CA50}^{\theta_{EVO}}-2*max\left(P_{HPfilt,j}\Big|_{\theta_{ST}}^{CA50}\right),0\right)}{2*max\left(P_{HPfilt,j}\Big|_{\theta_{ST}}^{CA50}\right)} \tag{2}$$

Additional performance parameters are defined by Heywood [10]. Combustion efficiency (η_{comb}) evaluates the fuel energy released relative to the total fuel energy injected ($m_f Q_{LHV}$). The unburned species mass measurements (m_i) in the numerator are measured with the Horiba emissions bench and $Q_{LHV,i}$ is the lower heating value of those respective species.

$$\eta_{comb} = 1 - \frac{\sum m_i Q_{LHV,i}}{m_f Q_{LHV}} \tag{3}$$

Net fuel conversion efficiency ($\eta_{f,x}$) is the thermodynamic work (W_x) divided by the total fuel energy that was injected into the cylinder. The subscript x refers to either indicated gross (*ig*), which evaluated over the compression and expansion strokes, or indicated net (*in*) which is evaluated over the entire cycle.

$$\eta_{f,x} = \frac{W_x}{m_f Q_{LHV}} \tag{4}$$

Thermal efficiency ($\eta_{th,x}$) is the thermodynamic work divided by the total fuel energy released. The equation incorporates combustion efficiency in the denominator to differentiate between fuel injected into the cylinder and fuel energy between fuel injected into the cylinder and fuel energy released. Like fuel conversion efficiency, the subscript x can be used for gross or net.

$$\eta_{th,x} = \frac{W_x}{m_f Q_{LHV} \eta_{comb}} \tag{5}$$

Indicated specific emissions (IS) of a species x is the mass flow rate of the species ($\dot{m}_x$) divided by the indicated power (P_i).

$$IS = \frac{\dot{m}_x}{P_i} \tag{6}$$

2.2 Outline of Steady-State Testing

Spark timing sweeps at six operating conditions were performed to evaluate TBC performance. At each operating condition, the spark timing was advanced in 3-degree increments until either the maximum brake torque (MBT) or the KLSA was achieved. Four of the six operating conditions were knock limited (KL). The load was defined by the target net indicated mean effective pressure (IMEP_n) at the end of each sweep. The conditions are summarized in Table 3.

Table 3: Experimental operating conditions for steady state testing

Speed [RPM]	Load [bar]	KL / MBT
1200	8	KL
1500	4	MIT
1500	8	KL
1500	12	KL
1800	8	KL
2200	8	MIT

2.3 Outline of Cold-Start Tests

A cold-start schedule was programmed into LabVIEW to enable a repeatable testing regiment. The schedule was primary focused on keeping unburned hydrocarbon emissions below the instrument saturation point (12,000 ppm) and avoiding complete misfires. The first four cycles motor (i.e., compress and expand air with no fuel injected) before the first firing cycle. The spark timing changed during the next six cycles to promote a suitable environment for complete combustion. The engine was slightly throttled to 90 kPa at an engine speed of 1300 RPM. Each individual cold-start test was 500 cycles long (46 seconds).

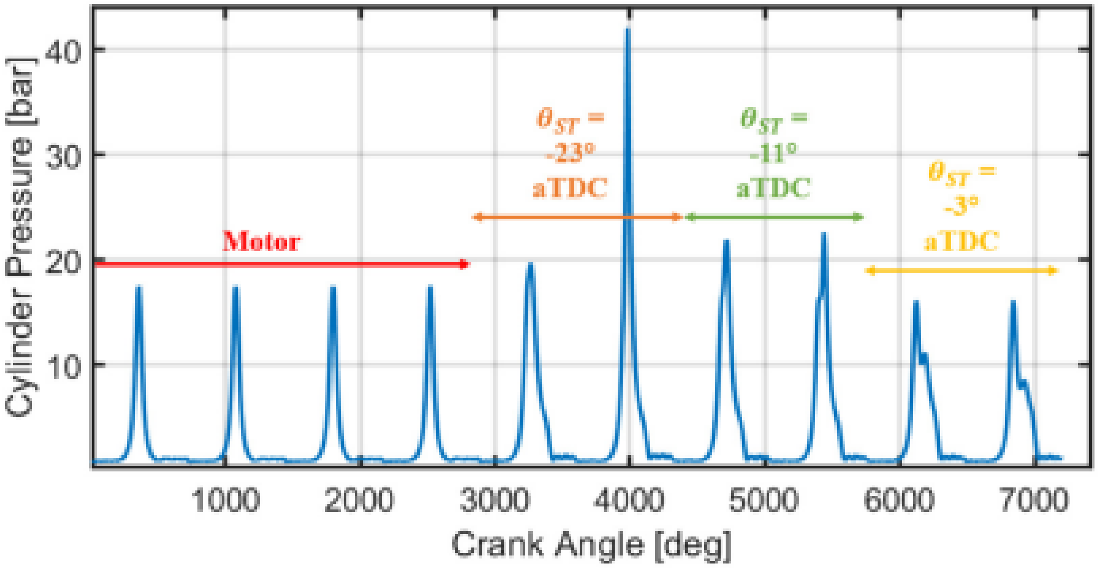

Figure 3: Cold-start spark time schedule over the first 10 cycles. The spark timing (Θ_{ST}) change was to ensure there were no complete misfires.

Particulate matter (PM) was recorded for each test through a Cambustion DMS500. This differential mobility spectrometer flows charged soot particles between 5 and 1000 nm through a classifier column where the particle's charge to aerodynamic drag ratio determines where the particle falls along the column [42]. Current measurements from electrometers along the column quantify the particle number and concentration. A total of eight cold-start tests were performed with each piston to generate a clear trend in emissions ensure repeatability. Coolant, oil, and air temperatures were maintained at 304 K, 314 K, and 298 K respectively, before the start of each test to ensure uniformity.

2.4 Coated Components Tested

A total of five coated pistons were tested. The TBCs were applied on aftermarket flat-top, hypereutectic pistons. Four pistons were coated with a novel, proprietary low thermal inertia material (referred to as NC) and one with gadolinium zirconate (GZO). The NC coating is a member of the LAMOX family characterized by low thermal conductivity and high coefficients of thermal expansion. GZO has been identified as a substitute for YSZ due to its lower thermal conductivity. GZO has been successfully tested in conventional diesel combustion [43] and advanced combustion modes [44]. One of the NC-coated pistons had a catalytically active topcoat applied (referred to as CCC). The seal coat was custom made using a commercial alkali binder and CCC (Ce:CO:Cu = 5:5:1) composite powder. This seal coat was applied via air-brush and air dried until fully cured. After the curing process, the thickness of the CCC topcoat was optically measured to be approximately 11-microns. A Fischer MP20 Dualscope with an ETA3.3H nonferrous probe was used to measure coating thickness. This nonferrous probe uses an energizing current to induce eddy currents through the material, with the magnitude of the eddy current being a function of the distance between the probe and aluminum substrate [45]. The instrument uncertainty was 0.5% of the measurement. Ten measurements were averaged across different locations along the piston surface. Total coating thicknesses are provided in Table 4. Note that the listed thicknesses include a bond coat thickness of ~50 microns.

Table 4: Coated piston thickness

Piston / Label	Thickness [µm]
Metal	--
120 µm NC	128.7 ± 8.7
200 µm NC	192.5 ± 12.2
200 µm NC w/ CCC	214.4 ± 22.9
200 µm GZO	206.8 ± 12.2
375 µm NC	375.9 ± 28.0

The engine coolant jug was shimmed up according to the measured thickness to compensate for differences in compression ratio. All coatings were sprayed with the air plasma spray (APS) thermal spray process. Thermal conductivity, specific heat capacity, and density of the baseline metal piston and TBCs are shown in Table 5.

Table 5: Thermophysical properties of baseline aluminum piston, NC, and GZO TBCs and the catalytically active topcoat (CCC)

Thermophysical Property	Baseline Aluminum Piston	NC	GZO	CCC
Thermal Conductivity [W/m/K]	100	0.59	0.95	0.30
Specific Heat Capacity [J/kg/K]	906	554	402	509
Density [kg/m^3]	2700	2996	6250	2240

Once the best performing piston was identified, valves coated with GZO on the front and backsides were installed to evaluate the contribution of each valve to system performance. The combustion face and backside of the intake and exhaust valves were coated with GZO because the coefficient of thermal expansion closely matched the steel valves compared to the NC coating. The coated valves are shown in Figure 4. All four valves were sprayed together and the thicknesses of each coated section are listed in Table 6. Note that the listed thickness also include a bond coat thickness of ~50 microns.

Figure 4: Gadolinium zirconate (GZO) coated combustion face, backside and stem of intake and exhaust valves

Table 6: Total thicknesses of combustion face, backside, and stem of both intake and exhaust valves

Section of Valve	**Baseline Aluminum Piston**

Combustion Face	207.7 ± 17.7
Backside	222.6 ± 18.9
Stem	131.3 ± 11.2

2.5 Outline of Durability Test

To understand the impact of CCD growth on low thermal inertia coatings, a pseudo-durability test was performed with a coated piston (200-micron NC piston) and coated heat flux probe (130-microns of NC coating). The heat flux probe was made from 316 stainless steel from IR Telemetrics. The material properties of the stainless steel body of the heat flux probe (i.e., uncoated) are listed in Table 6. The heat flux probe had two J-type thermocouple junctions that are vapor deposited to allow for fast response temperature measurements. One junction was located on the surface of the probe, and the other is set back 2-mm into the probe (x_{hfp}). The coated heat flux probe thickness encompasses both TBC and CCD (x_{tbc}), which builds during the test. On the coated heat flux probe, the surface thermocouple junction measured the coating backside temperature ($T_{bs,tbc}$). An image of an uncoated heat flux probe and a schematic of the thermocouple junctions and thicknesses are shown in Figure 5.

Table 7: Material properties for the stainless steel body of the heat flux probes.

Thermal conductivity [W/m/K]	**16.2**
Specific heat [J/kg/K]	**490**
Density [kg/m^3]	**8000**

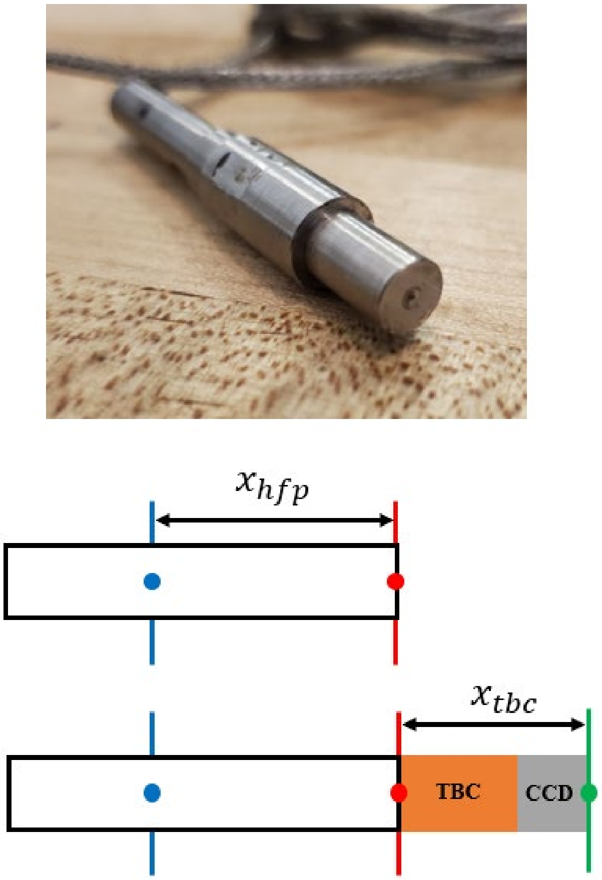

Figure 5: IR Telemetrics heat flux probe with schematic showing the location of temperature measurements.

First, the engine was run at a speed of 1500 RPM with a load of 4 bar IMEP_n to build up a layer of CCD on both the piston and coated heat flux probe. Every 12.5 hours, the coated heat flux probe was removed for thermal diffusivity and thermal conductivity measurements and a spark timing sweep was performed to determine the KLSA at a speed of 1500 RPM with a load of 8 bar IMEP_n. Once an equilibrium thickness was achieved on the coated heat flux probe (i.e., CCD no long grows), the engine was run at a speed of 2200 RPM with a load of 9 bar IMEP_n in order to remove the CCD layer. The EGAB1.3 ferrous probe with the Fischer MP20 Dualscope was used to measure the thickness of the TBC and CCD layer on the heat flux probe. A total of ten measurements were performed. The probe also has an uncertainty of 0.5%.

Diffusivity measurements were performed with a custom-built radiation chamber. More details on the construction and operation can be found in Reference [47]. The radiation chambers used a blackbody graphite heating element and a motor driven chopping wheel with two clots to impart a square wave radiative heat flux onto an uncoated and coated heat flux probe. Due to the coating, there was an observable phase lag difference between the surface temperature measurement of the uncoated heat flux probe and coating backside temperature measurement of the coated heat flux probe. Figure 6 shows the phase lag (Δt) between the uncoated and coated heat flux probes.

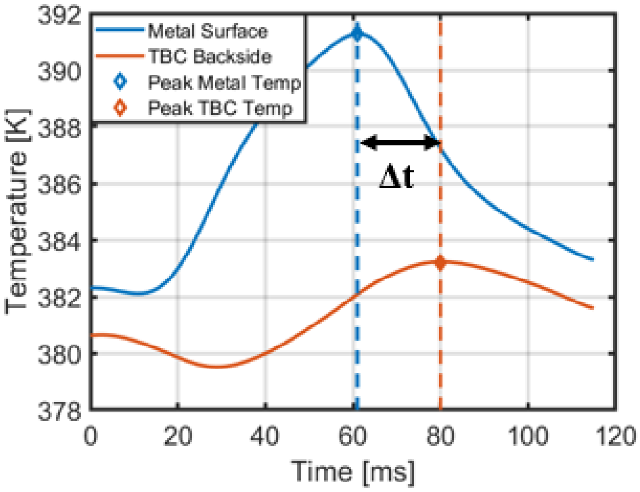

Figure 6: Temperature measurements from the same junction of two heat flux probes, with the coated probe experiencing a delayed response due to the presence of the coating.

Thermal diffusivity (α) was calculated using the correlation developed by Hopwood et al. in Equation (7), where Δt is the time difference between clean and coated temperature peaks and t_0 is the equivalent 4-stroke engine speed [48].

$$\alpha = \frac{{x_{tbc}}^2}{\Delta t^2}\frac{t_0}{\pi}(0.209)(1 - \frac{\Delta t}{4t_0})^{-2} \tag{7}$$

A thermocouple conditioner and amplifier from FusionDAQ was used for grounding and cold-junction compensation of the voltage inputs from the heat flux probes. Temperatures were measured in a custom LabVIEW program and processed in MATLAB. To reduce noise, several temperature pulses were selected and normalized on the same time axis. The temperature swings were averaged and passed through a low pass filter to smooth the signal. This process is summarized in Figure 7. Temperature measurements at motor speeds of 320, 480, and 640 RPM were recorded over a period of 5 minutes per test.

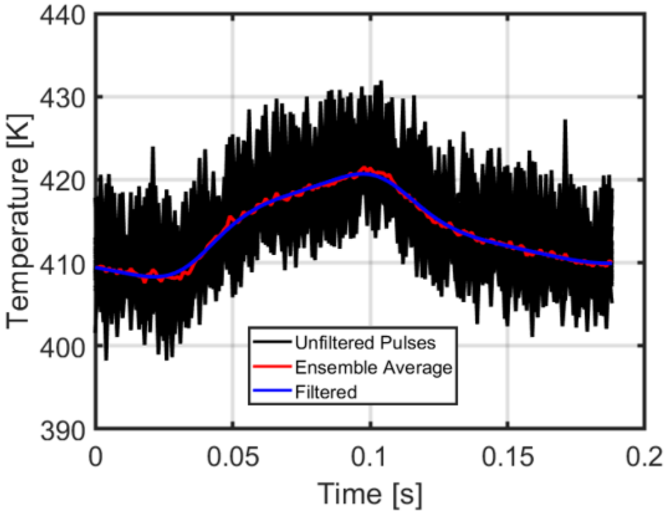

Figure 7: Processing of temperature data using an ensemble averaging routine at a motor speed of 640 RPM.

A custom rig was developed to measure conductivity of the coated heat flux probe. A heat gun blows hot air towards the surface of the probe while a Raytek infrared temperature sensor measures the surface temperature. Figure 8 shows the conductivity rig with marked components.

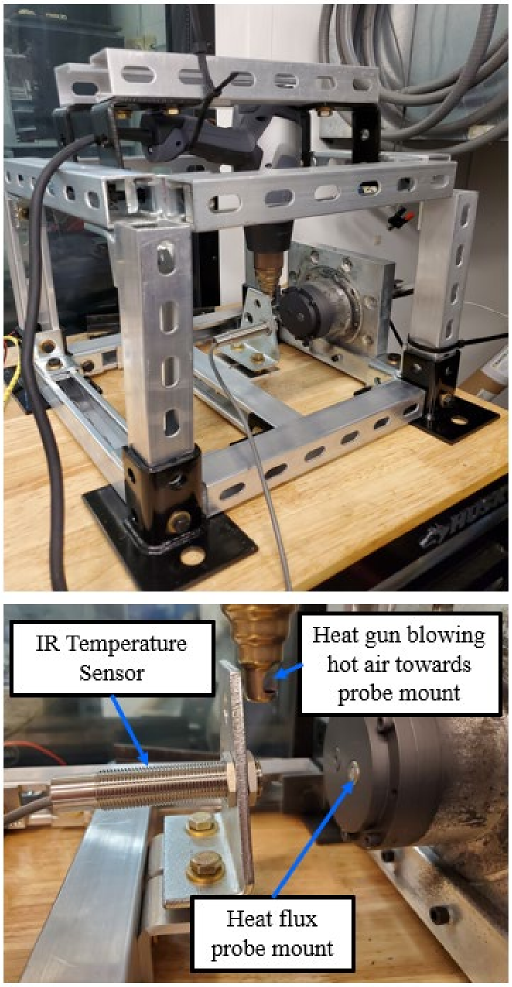

Figure 8: Conductivity rig with labelled components.

The heat flux probes and mount were sprayed with a layer of aerosol graphite to reduce the reflectivity and increase the emissivity of the surface to near unity such that the IR sensor's measurements were as accurate as possible. Because the view area of the IR temperature sensor was slightly larger than the targeted area, the temperature sensor was calibrated against the surface temperature of an uncoated heat flux probe. Once the IR probe's temperature measurement was pegged to the uncoated heat flux probe's surface temperature measurement, the coated heat flux probe was tested within the calibrated temperature change. Conductivity was calculated using the 1D heat diffusion equation:

$$\left(\rho c_p \frac{\partial T}{\partial t}\right)_y = \left(\frac{\partial}{\partial x}\left(k \frac{\partial T}{\partial x}\right)\right)_y \tag{8}$$

where $\frac{\partial T}{dt}$ is the time-based temperature difference and $\frac{\partial T}{dx}$ is the temperature change through the material. The subscript y refers to either the coated or steel section of the heat flux probe (tbc or hfp, respectively). Ideally, the conductivity would be calculated when equilibrium was achieved throughout the entire heat flux probe, i.e., when $\frac{\partial T}{dt} = 0$. However, it was found that the temperature of the heat flux probes continued to rise slowly even after a period of more than an hour by experimenting with the conductivity rig. However, if $\frac{\partial T}{dt}$ is constant, then analytical solution can be found. Since the heat flux from the coating surface to coating backside was equal to the heat flux from the coating backside to the backside temperature junction (set 2-mm back) at the interface between the coating and metal, the following equation can be obtained:

$$k_{tbc} = \frac{\frac{1}{2}\left(\rho c_p\right)_{hfp}\left(\frac{\partial T}{\partial t}\right)_{hfp} x_{hfp} + \frac{k_{hfp}}{x_{hfp}}\left(T_{b,tbc} - T_{b,hfp}\right)}{\frac{T_{s,tbc} - T_{b,tbc}}{x_{tbc}} - \frac{x_{tbc}}{2\alpha_{tbc}}\left(\frac{\partial T}{\partial t}\right)_{tbc}} \tag{9}$$

where $T_{s,tbc}$ is the coating surface temperature measured via IR temperature sensor and $T_{b,hfp}$ is the heat flux probe backside temperature (measured from the junction 2-mm back from the probe surface junction). TBC diffusivity (α_{tbc}) was measured through the radiation chamber. This conductivity measurement was intended to provide information regarding relative changes in TBC conductivity due to CCD growth.

2.6 Uncertainty Analysis

Uncertainty analysis was performed according to the guidelines set up by Gainey et al [49]. A 95% confidence interval was propagated using Equation (10). where ∂z_{x_i} is the sensitivity coefficient of z to x_i (i.e. the partial derivative of z with respect to x_i), σ_{x_i} and σ_z are the uncertainty of x_i and z, respectively, $\sigma_{x_i x_j}$ is the covariance of the two variables x_i and x_j, σ_{meas} is the measurement uncertainty of z, and $\sigma_{z,instr}$ is the instrument uncertainty of z. If z is calculated, the last two terms in Equation (10) are omitted. If z is directly measured, the first two terms in Equation (10) are omitted.

$$\sigma_z^2 = \sum_{i=1}^{n} \partial z_{x_i}^2 \sigma_{x_i}^2 + 2\sum_{i=1}^{n-1} \sum_{j=i+1}^{n} \partial z_{x_i} \partial z_{x_j} \sigma_{x_i x_j} + \sigma_{z,meas}^2 + \sigma_{z,instr}^2 \tag{10}$$

For the diffusivity test, the most significant source of uncertainty was the thickness measurement. Because the heat flux probe diameter was smaller than the measuring probe diameter, the standard deviation across the ten measurements was high. Since diffusivity was calculated from phase lag (in seconds or milliseconds), additional uncertainty stems from the encoder resolution. An optical encoder with a 0.1 crank angle resolution was used, which provided a phase lag uncertainty of ± 0.05 crank angle.

For the conductivity test, the thickness uncertainty was non-negligible, but the small temperature difference between the temperature measurements produced uncertainties equal to or greater than the calculated conductivity value. It was impractical to increase the temperatures enough to lower the conductivity uncertainty below 1 W/m/K, with a required temperature difference of 5 K shown in Figure 9. As will be shown in the results, the conductivity uncertainty decreases as the temperature difference increased.

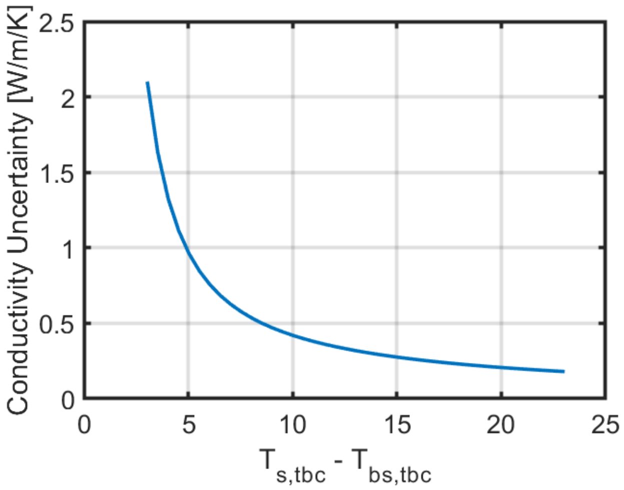

Figure 9: Conductivity uncertainty vs. coating surface and backside temperature difference.

CHAPTER 3. COATED PISTON RESULTS

The first sections (referred to as Thick Pistons) will analyze all pistons except the 120-micron NC piston, since it was tested with a different batch of EPA Tier III gasoline with a slightly different octane number. The results for the 120-micron NC piston are shown in the Thin Piston section with its own metal baseline for fair comparison.

3.1 Thick Pistons: Speed Sweep – 8 bar

Net thermal efficiency, knock intensity, and combustion efficiency at 1200 RPM, 1800 RPM, and 2200 RPM are shown Figure 10. The performance behavior at 1200 RPM underscores the challenges associated with TBCs in SI. At a CA50 of ~15 degrees after TDC, the 200-micron NC piston achieved a net thermal efficiency of 36.38% ± 0.21% compared to 36.27% ± 0.21% of the metal baseline. Thus, at the same spark timing, the TBC achieved an efficiency gain of 0.11% ± 0.42%. However, the KLSA of the 200-micron NC piston had a 1.5 degree spark timing retard compared to the metal baseline. Comparing the metal and 200-micron NC pistons at their respective KLSA timings, the net thermal efficiencies were statistically identical 36.97% ± 0.21% and 36.95% ± 0.21%, respectively, resulting in no overall efficiency improvement. The severity of the knock penalty is further illustrated at 2200 RPM, where the 200-micron and 375-micron NC piston almost reached the 100% knock intensity limit even though the metal piston and other coated pistons were still well below the knock intensity limit.

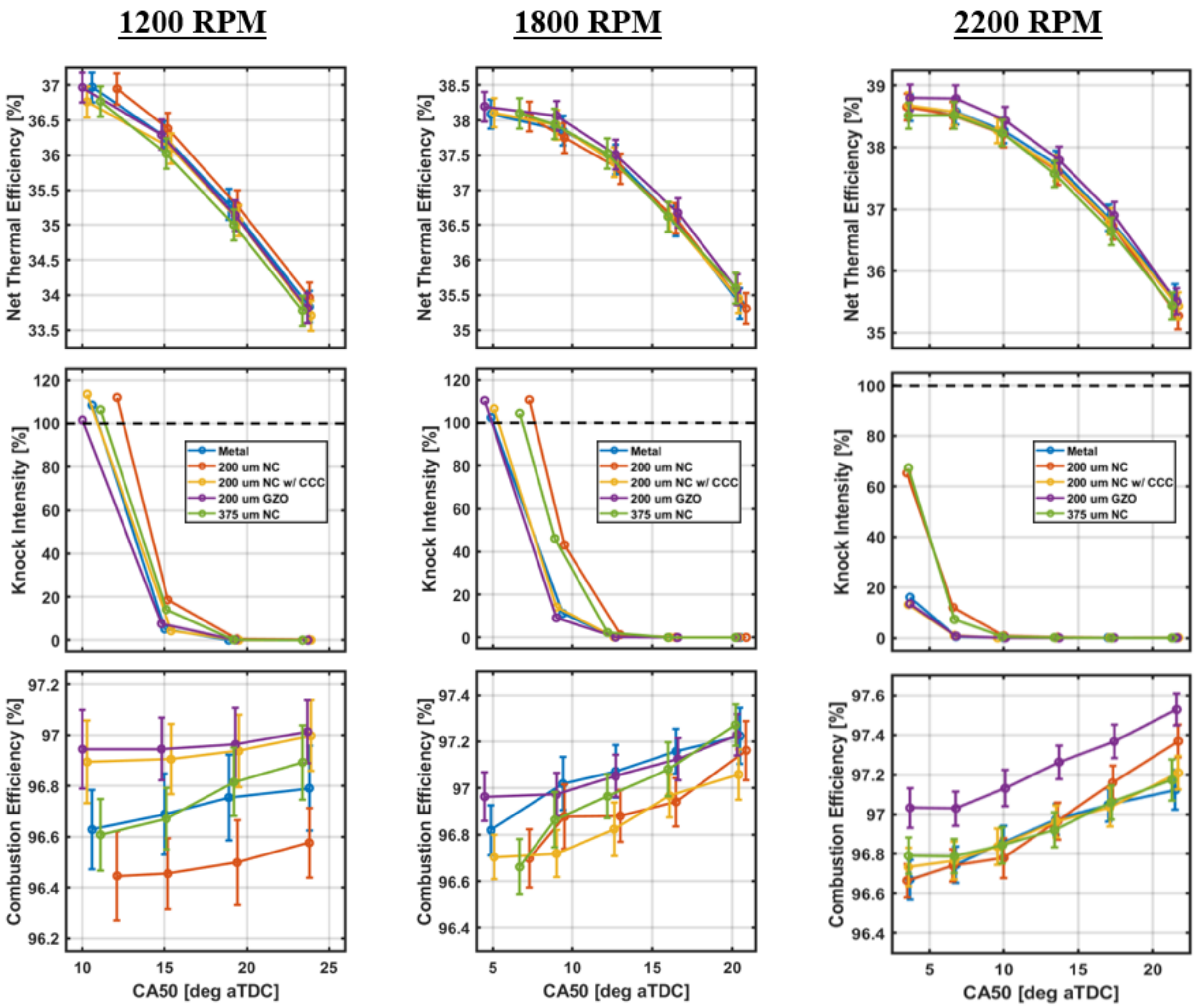
1200 RPM

1800 RPM

2200 RPM

Figure 10: Net thermal efficiency, knock intensity, and combustion efficiency of the thick piston set at 1200 RPM, 1800 RPM, and 2200 RPM at 8 bar IMEP$_n$. The black dashed line represents the KLSA limit.

The 200-micron NC w/ CCC piston closely matched the knocking behavior of the baseline piston, despite the 200-micron NC piston experiencing a significant knock penalty. Since the only difference between the two pistons was the surface layer, it was likely that the topcoat changed the thermophysical properties of the coating system, which produced these different responses at the tested operating conditions. Seal coats on top of TBCs have been shown to significantly impact the conductivity and diffusivity of the overall coating system [50]. According to Table 5, the thermophysical properties of the catalytically active topcoat are superior to both the NC and GZO coatings, suggesting that even a low thickness of ~10-microns was enough to decrease the thermal inertia of the piston surface and improve the performance of the TBC.

The 200-micron GZO piston was the only TBC to achieve a comparable or slightly higher net thermal efficiency than the metal baseline as the KLSA either matched or slightly advances relative to the metal piston. At 1200 RPM, the 200-micron GZO piston matched the baseline net thermal efficiency of 36.97% ± 0.21%. At 1800 RPM and 2200 RPM, the 200-micron GZO piston experienced a net thermal efficiency increase of 0.11% ± 0.41% and 0.16% ± 0.42% over the baseline, respectively.

There was no significant change in combustion efficiency with the application of these TBCs in these experiments. The 200-micron GZO piston was the only coated piston with a higher combustion efficiency than the metal piston across multiple speeds. All other coated pistons were not consistent and within the uncertainty bands of the metal baseline. The indicated specific unburned hydrocarbon and CO emissions are provided in Figure 11. The unburned hydrocarbon emissions decreased, and CO emissions increased with the application of these TBCs. It is unclear why the emissions behaved this way, but the literature also shows mixed emissions results. Assanis and Mathur recorded slightly higher CO emissions [14], whereas Moughal and Samuel showed reductions in both unburned hydrocarbon and CO emissions in a two-stroke SI engine [51]. Chérel showed that despite a ~1.3 percentage point increase in combustion efficiency, unburned hydrocarbon emissions increased with TBCs [23]. Chérel specifically referenced the coating porosity the source of higher unburned hydrocarbon emissions. Excessive porosity could behave like a crevice storing fuel within the coating and releasing the fuel during the expansion stroke, causing late stage oxidation and higher unburned hydrocarbons. However, the low porosity of the

TBCs in this thesis (~10%) and the decline in unburned hydrocarbon emissions suggest that fuel storage within the coating was not present during these experiments.

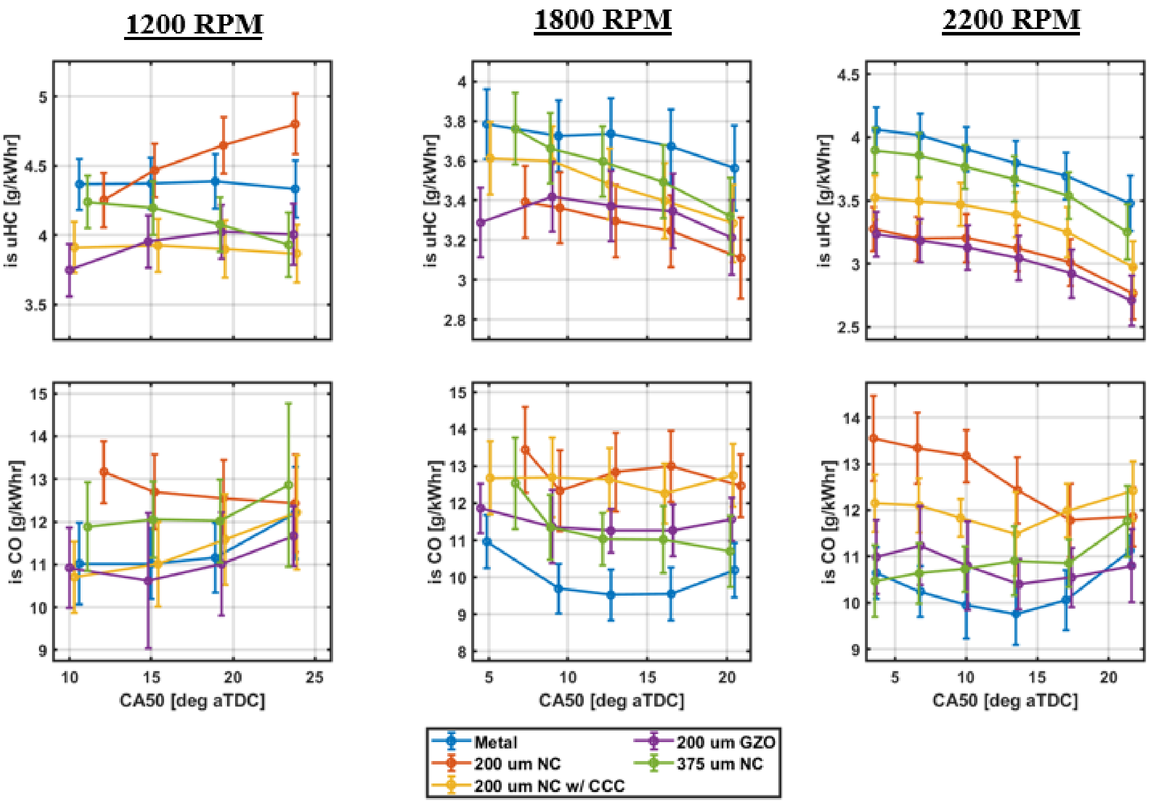

Figure 11: Indicated specific unburned hydrocarbon (is uHC) and carbon monoxide (is CO) emissions at 1200 RPM, 1800 RPM, and 2200 RPM at 8 bar IMEP$_n$.

It is also important to note that the catalytically active coating (200-micron NC w/ CCC piston) did not achieve a statistically significant reduction in emissions compared to the other coated pistons. Researchers have shown success with the application of catalytically active coatings within the combustion chamber. Hu and Ladommatios demonstrated a 20% reduction in unburned hydrocarbons with the application of a platinum-rhodium coating applied on the piston crown [52]. Haenel et al. coated the cylinder head and pistons of a production 2.0 liter, 4-cylinder SI engine with titanium dioxide and found a large reduction in unburned hydrocarbon emissions, but no statistically significant change in CO emissions under stoichiometric conditions [53].

Powell tested the CCC top layer on the surface of a YSZ piston and found a higher combustion efficiency compared to normal YSZ in HCCI [54]. Considering that the CCC topcoat had been shown to work successfully in HCCI, it is believed that the vastly different combustion mode was the source of these differences. In HCCI, the combustion efficiency is nominally low because cold regions in the cylinder never reach auto-ignition temperatures, causing high unburned hydrocarbon and CO emissions. Thus, there is more opportunity to promote catalytic reactions when the reductant is widely available. Additionally, oxygen is more readily available for catalytic reactions under the globally lean operation of HCCI, whereas stoichiometric, direct injected SI has more pronounced equivalence ratio stratification regardless of injection timing [55].

3.2 Thick Pistons: Load Sweep – 1500 RPM

Net thermal efficiency, knock intensity, and combustion efficiency versus CA50 for the 4 bar, 8 bar and 12 bar $IMEP_n$ operating conditions are shown in Figure 12. The 4 bar $IMEP_n$ operating condition does not have the knock intensity plot because it was not knock limited. The trends in net thermal efficiency and knock intensity were similar to those observed during the speed sweep in Figure 10. At the two knock limited conditions of 8 bar and 12 bar $IMEP_n$, the 200-micron NC and 375-micron NC pistons were severely knock limited and experienced a CA50 retard of 1.7 and 1.2 degrees relative to the baseline, respectively. In terms of net thermal efficiency, this was an especially large penalty at 12 bar $IMEP_n$ where small changes in CA50 significantly impact efficiency. Detailed efficiency numbers and heat release parameters are shown in Table 8 at KLSA for the 1500 RPM, 12 bar $IMEP_n$ operating condition. The 200-micron NC and 375-micron NC pistons required a spark timing retard of 1.3 degrees to maintain the same knock intensity as the baseline metal, resulting in a decrease in gross and net thermal and fuel conversion efficiency. However, the 200-micron GZO and 200-micron NC w/ CCC pistons closely matched the KLSA of the metal baseline, which allowed those two pistons to closely match or slightly exceed the uncoated efficiency.

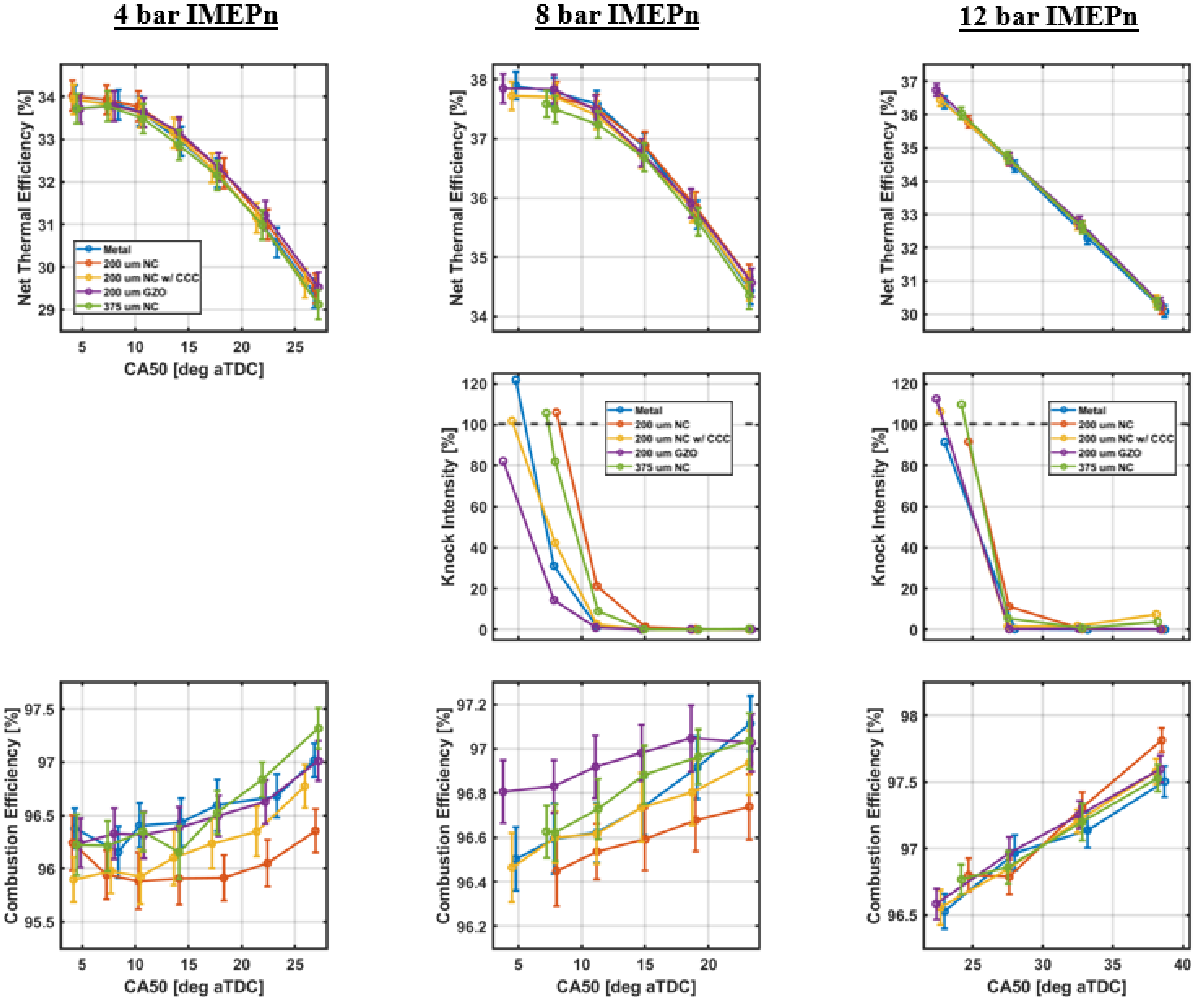

Figure 12: Net thermal efficiency, knock intensity, and combustion efficiency of the thick piston set at 4 bar, 8 bar, and 12 bar IMEP$_n$ at an engine speed of 1500 RPM. The black dashed line represents the KLSA limit. Note that 4 bar IMEP$_n$ does not have knock intensity because that operating condition was not knock limited.

Table 8: Performance results of baseline and coated pistons at KLSA at 1500 RPM, 12 bar IMEP$_n$.

	Metal	200 µm NC	200 µm NC w/ CCC	200 µm GZO	375 µm NC
Spark Timing [deg aTDC]	-6.9	-5.6	-6.7	-7.0	-5.6
IMEP$_n$ [bar]	11.8 ± 0.1	11.5 ± 0.1	11.8 ± 0.1	11.8 ± 0.1	11.6 ± 0.1
Comb. Eff. [%]	96.5 ± 0.1	96.8 ± 0.1	96.6 ± 0.1	96.6 ± 0.1	96.8 ± 0.1
CA10 [deg aTDC]	12.6 ± 0.2	14.2 ± 0.2	12.6 ± 0.2	12.3 ± 0.2	13.7 ± 0.2
CA50 [deg aTDC]	23.0 ± 0.1	24.7 ± 0.1	22.7 ± 0.2	22.4 ± 0.1	24.2 ± 0.1
CA90 [deg aTDC]	40.9 ± 0.5	41.4 ± 0.5	40.3 ± 0.5	38.3 ± 0.5	41.4 ± 0.5
NTE [%]	36.4 ± 0.2	35.8 ± 0.2	36.4 ± 0.2	36.7 ± 0.2	36.0 ± 0.2
GTE [%]	36.8 ± 0.2	36.1 ± 0.2	36.8 ± 0.2	37.1 ± 0.2	36.5 ± 0.2
NFCE [%]	34.9 ± 0.2	34.4 ± 0.2	35.0 ± 0.2	35.3 ± 0.2	34.7 ± 0.2
GFCE [%]	35.3 ± 0.2	34.8 ± 0.2	35.3 ± 0.2	35.6 ± 0.2	35.1 ± 0.2

At 4 bar IMEP$_n$, the net thermal efficiency across all coated pistons were within uncertainty at maximum brake torque timing (MBT). The combustion efficiency of the coated pistons at this low load operating condition was notably lower than the uncoated baseline. This decline in combustion efficiency was driven by high unburned hydrocarbon emissions. This is shown in Figure 13 which displays the indicated specific unburned hydrocarbon emissions across the load sweep. The coated pistons generated higher unburned hydrocarbon emissions than the metal baseline at the lowest load of 4 bar IMEP$_n$. At 8 bar and 12 bar IMEP$_n$, the unburned hydrocarbon emissions were either lower or roughly equal to the baseline. If the pores of the TBCs were behaving like a crevice, higher unburned hydrocarbon emissions would be expected at higher loads where the elevated cylinder pressure would force more fuel into the coating. However, it is unclear why the unburned hydrocarbon emissions were broadly higher than the baseline only at 4 bar IMEP$_n$.

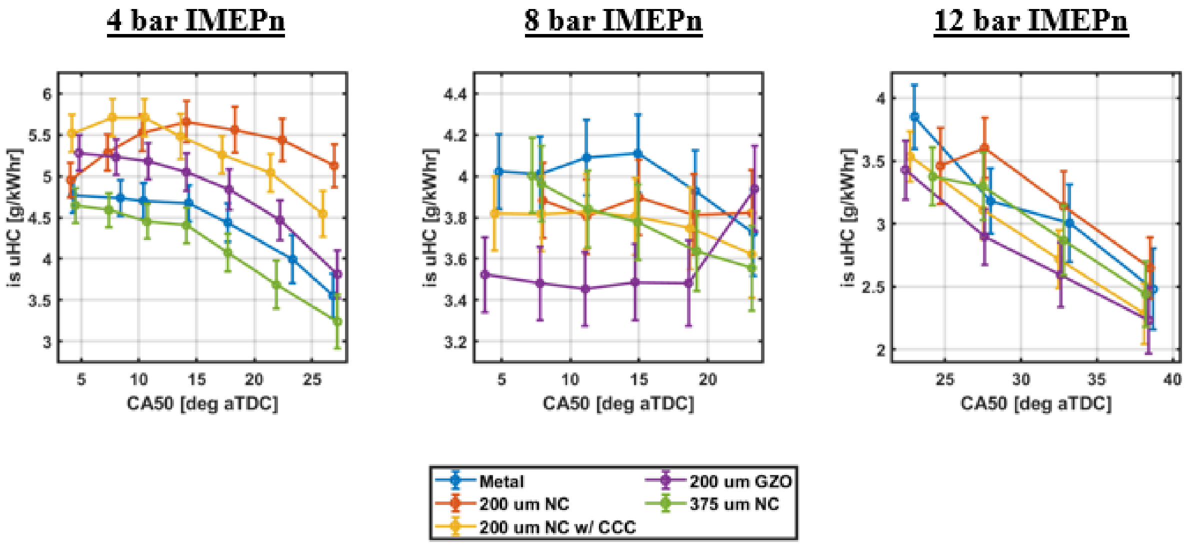

Figure 13: Indicated specific unburned hydrocarbon (is uHC) emissions at 4 bar, 8 bar, and 12 bar IMEP$_n$ at an engine speed of 1500 RPM.

Exhaust temperature 4 bar, 8 bar and 12 bar IMEP$_n$ operating conditions are shown in Figure 14. Surprisingly, the exhaust temperatures were generally lower with all coated pistons except for the 375-micron NC piston. This result is contrary to simulation [56] and experimental results [14] which have shown higher exhaust gas temperatures with TBCs. In this experiment, the exhaust temperature was measured by a thermocouple mounted in the exhaust runner with its tip pointed into the exhaust port. Since these coatings use low volumetric heat capacity to prevent excess heat storage in the TBC, it is possible that the transient nature of the surface temperature does not effectively increase exhaust gas temperature. Additionally, since this study focuses on relatively thin coatings applied only to the piston, the coated surface area fraction may not be large enough to produce a significant increase in exhaust temperature.

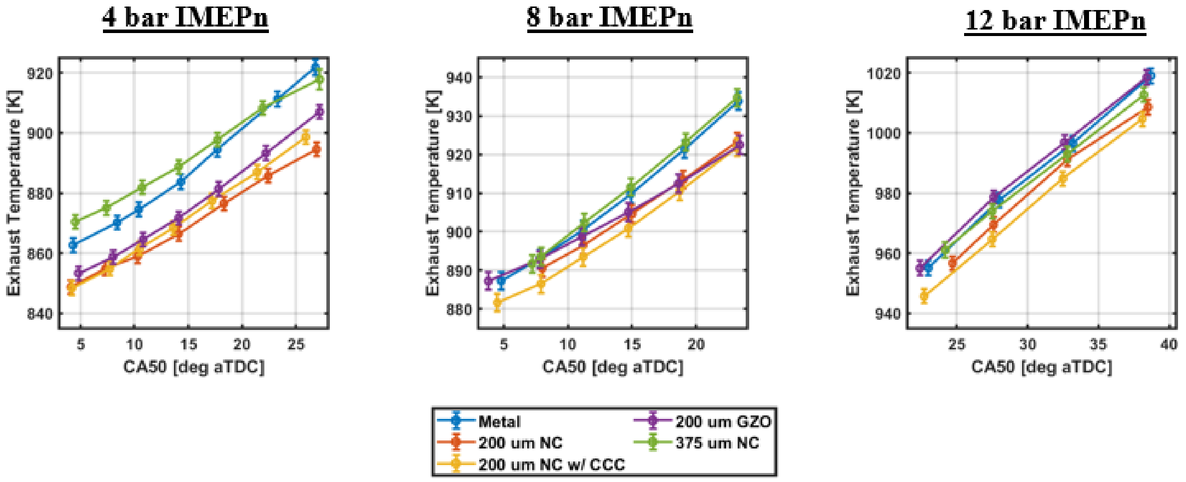

Figure 14: Exhaust temperature at 4 bar, 8 bar, and 12 bar IMEP$_n$ at an engine speed 1500 RPM.

As it stands, without an increase in either efficiency or exhaust temperature, these results imply that no heat transfer reduction was achieved in the 200-micron NC and 375-micron NC pistons. Yet the increase in knock propensity demonstrated in these results indicate that the surface temperature of the piston was elevated and charge heating occurred. Parallel thermodynamic modelling work on the impact of low thermal inertia TBCs in SI demonstrated modest, but non-negligible increases in efficiency and exhaust temperature (<1% relative efficiency gain, 10-15 K exhaust temperature increase) [57]. While previous research has highlighted that this could result from increased surface roughness of the TBC compared to a metal piston [58], the TBCs in this work were polished such that their surface roughness was below 2 microns Ra (roughness average). Additional phenomena such as convection vive or decreased flame quenching length can not be easily confirmed through analysis of experimental data as they pertain to thermal boundary layer effects. Additional imperfections in the TBC such as surface porosity could contribute to the results shown here. Engine rebuild uncertainty is difficult to quantify and control, but in this study where efficiency uncertainty is within three-tenths of a percentage point, the piston swap process could introduce some variability. However, the general spread of the presented results suggest that this variability was minimized.

Since the air flow controller maintains the same air flow rate by changing the intake pressure, charge heating could be observed by analyzing the intake pressure trace under firing conditions. A crank resolved intake pressure trace at a spark timing of -3 degrees aTDC at 1500 RPM, 12 bar $IMEP_n$ is shown in Figure 15. Even though some of the intake pressure differences can be characterized by instrument uncertainty, rebuild uncertainty, and day to day variation, the results generally align with the knock observations from the experimental data. The 200-micron NC piston experienced a slight increase in intake pressure, which suggests that with the same mass of air entering the cylinder, charge heating elevated the intake pressure. The exception to this behavior was the 375-micron NC piston, which had lower intake pressure compared to the uncoated condition. But considering there was a knock penalty using this piston at all tested operating conditions, it is likely that charge heating also occurred. The intake pressure traces of the 200-micron NC w/ CCC piston closely matched the intake pressure trace of the uncoated piston, and the 200-micron GZO piston had a slightly lower intake pressure. Considering that there was no observable knock penalty with these two pistons, there was likely no charge heating.

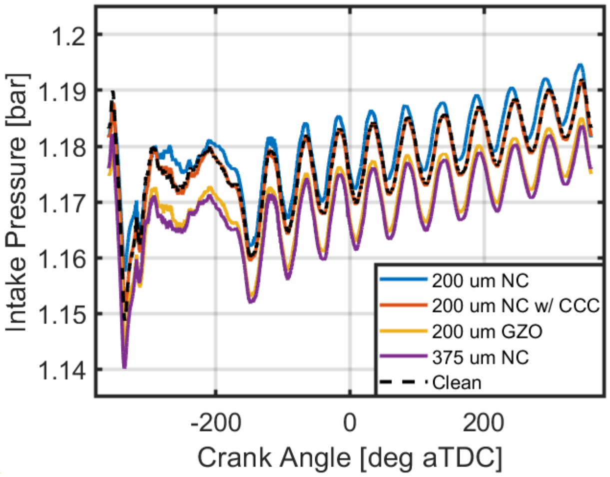

Figure 15: Average intake pressure vs. crank angle at a spark timing of -3 degrees aTDC at 1500 RPM, 12 bar IMEP$_n$.

3.3 Thin Piston Results

The above results demonstrated a deterioration in the performance of the NC coating with thicknesses greater than 200-microns. The excessive thickness contributes to charge heating during the intake stroke, which increased knock propensity. However, an extremely thin coating may not produce a temperature swing large enough to produce a statistically significant impact. The penetrative depth of a coating is the thickness at which the temperature swing of a coating is maximized without a bulk temperature shift [59]. Any additional thickness greater than the penetrative depth contributes to charge heating as the sub-layers store heat rather than swing like the layers close to the surface of the coatings. Penetrative depth is a function of the thermophysical properties of the coating and the engine speed. At 1500 RPM, the penetrative depth of the NC material is ~120-microns. Therefore, it is of interest to study the performance of a coating roughly equal to the penetrative depth. Performance results of this thin piston are shown in Figure 16 and Figure 17.

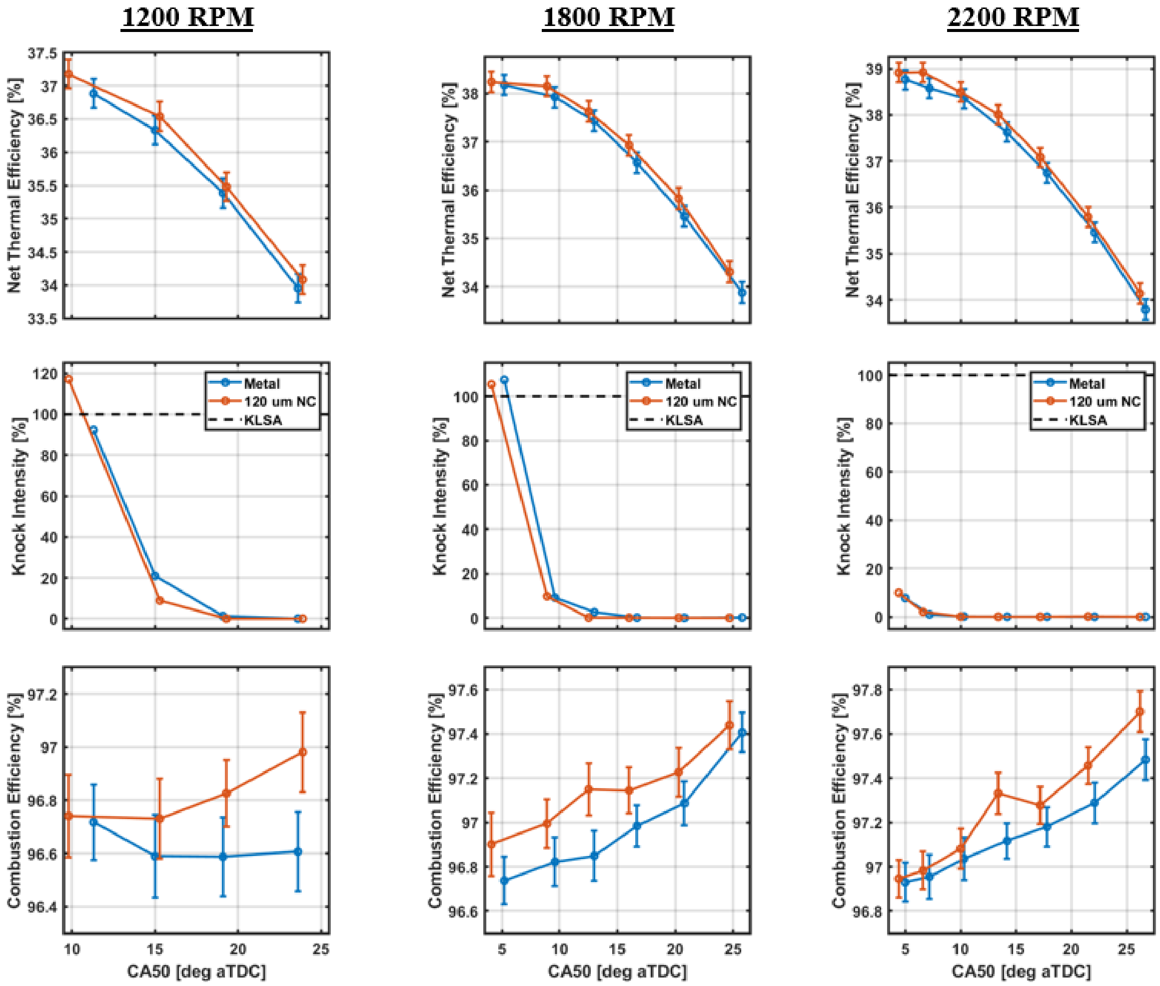

Figure 16: Net thermal efficiency, knock intensity, and combustion efficiency of the thin piston (120-micron NC piston) at 1200 RPM, 1800 RPM, and 2200 RPM at 8 bar IMEP$_n$. The black dashed line represents the KLSA limit.

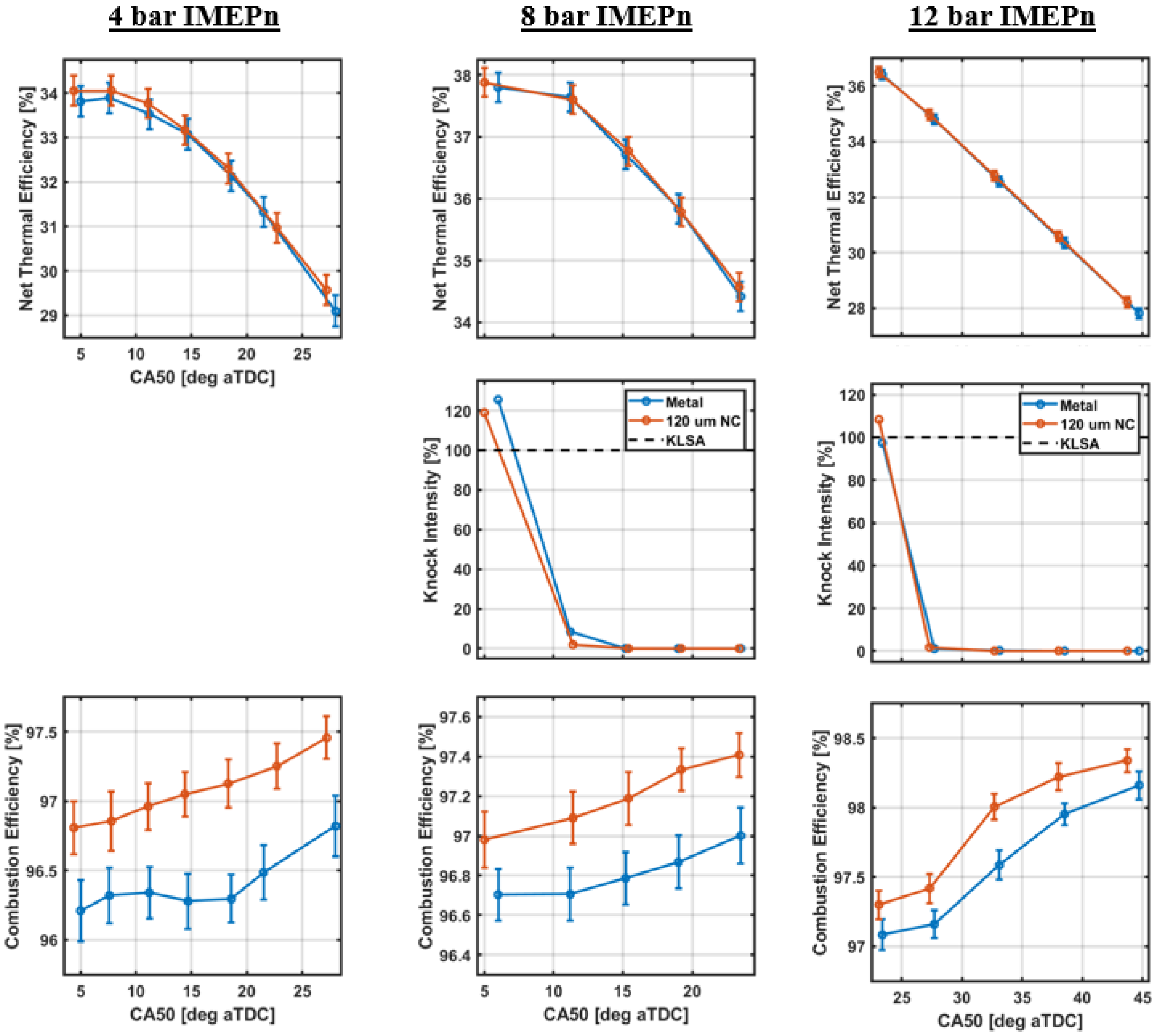

Figure 17: Net thermal efficiency, knock intensity, and combustion efficiency of the thin piston (120-micron NC piston) at 4 bar, 8 bar, and 12 bar IMEP$_n$ at an engine speed of 1500 RPM. The black dashed line represents the KLSA limit. Note that 4 bar IMEP$_n$ does not have knock intensity because that operating condition was not knock limited.

The 120-micron NC piston experienced a slight KLSA extension at knock limited operating conditions, which allowed the net thermal efficiency to increase through further spark advance. This implies that there was a charge cooling effect that effectively countered the increased knock propensity induced by blocking heat transfer during combustion. The combustion efficiency was also higher than the metal piston across all tested operating conditions. It is unclear what drove the increase in combustion efficiency compared to the other NC pistons. Figure 18 shows the intake pressure trace under the same air flow rate under firing conditions. Similar to the 200-micron GZO piston in Figure 15, the lower intake pressure implies the surface temperature of the coating cooled below that of the metal piston.

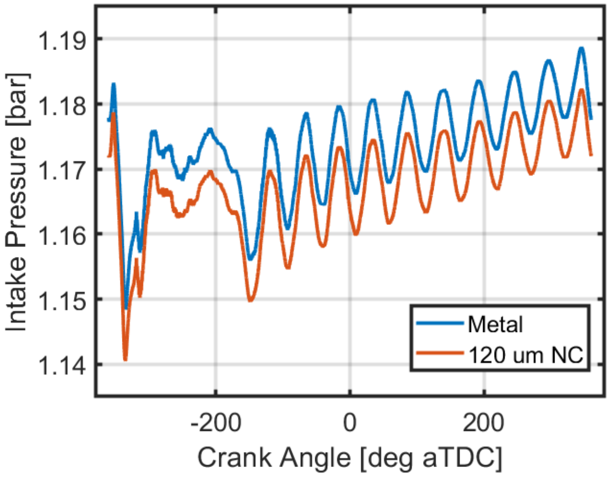

Figure 18: Average intake pressure vs. crank angle at a spark timing of -3 degrees aTDC at 1500 RPM, 12 bar IMEP$_n$.

At 1200 RPM (Figure 16) at a CA50 of ~15 degrees after TDC, the net thermal efficiency of the 120-micron NC piston and metal baseline was 36.54% ± 0.22% and 36.33% ± 0.22%, respectively. At this spark timing, the 120-micron NC piston produced an efficiency gain of 0.21% ± 0.44%, which was higher than the 0.11% ± 0.42% gain of the 200-micron piston in Figure 10. When factoring in the advance in KLSA, the efficiency gain of the 120-micron NC piston was 0.30% ± 0.44% compared to essentially zero efficiency change with the 200-micron piston. The efficiency change remained higher at 2200 RPM, albeit with evidence of diminishing returns as the total cycle time decreased. This agrees with previous studies showing a dependence on engine speed with TBCs since heat transfer is time based [14], [60]. The sudden deterioration in efficiency from 120-microns to 200-microns indicates a significant penalty with increasing thickness past the penetrative depth in SI, both from a knock and efficiency perspective.

3.4 Cold Start Results

The average particulate distributions from eight cold-start tests for each piston are provided in Figure 19. The particulate distributions were cut off at 365 nm because there was no observable soot formation past those diameters. Adding a TBC significantly reduces the number of fine particles (diameters less than ~30 microns). The reduction in fine particles is particularly beneficial from a human health perspective since small particles can easily penetrate the bloodstream [61]. PM formation in SI during cold-starts is primarily attributed to liquid pool fires on the combustion chamber surfaces [62]-[64]. The low thermal inertia of the TBCs should allow a more rapid increase in surface temperature to evaporate gasoline off the piston, minimizing pool fires and reducing PM emissions. Note that this engine uses a centrally mounted direct injector, which contributes to higher PM emissions compared to other fuel delivery systems, such as port-fuel injection (PFI) [65].

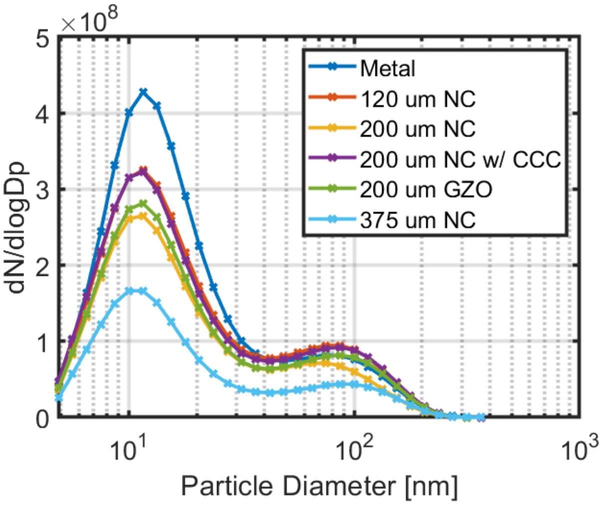

Figure 19: Average particulate distribution vs. particle diameter of eight cold-start tests.

The particle concentration and mass median diameter (i.e., diameter at which 50% of the mass is contained in smaller and larger particles) is shown in Table 9. Since there was no known instrumentation uncertainty, the error was propagated with a 95% confidence interval using the standard deviation of the eight cold-start tests. A plot of each individual test is provided in APPENDIX A.

Table 9: Average particle concentration and mass median diameter of the metal baseline and coated pistons during eight simulated cold-start tests.

Piston	**Particle Concentration [ng/cm^3]**	**Mass Median Diameter [nm]**
Metal	31.4 ± 7.0	145.2 ± 1.9
120 µm NC	33.9 ± 6.2	140.9 ± 2.0
200 µm NC	21.1 ± 1.4	135.4 ± 3.2
200 µm NC w/ CCC	35.0 ± 3.7	143.4 ± 1.8
200 µm GZO	31.4 ± 3.3	143.8 ± 1.1
375 µm NC	19.0 ± 3.1	149.1 ± 3.6

Compared to the metal piston, the particle concentration was unchanged or slightly higher with the 120-micron NC, 200-micron NC w/ CCC, and 200-micron GZO pistons, despite the non-negligible decrease in fine particles in Figure 19. Larger particles will contribute more to the particle concentration, thus a small increase in the number of larger particles outweighed the modest decrease in finer particles. In contrast, the 200-micron and 375-micron NC coatings substantially reduced PM emissions. A possible explanation is that these coatings experience a bulk shift in the surface temperature, which was evidenced by the retarded KLSA at the knock limited operating conditions during steady-state testing. Thus, the elevated surface temperature of these coatings during the intake stroke allowed more fuel to evaporate off the piston surface during the cold-start.

Exhaust temperature and unburned hydrocarbons are shown in Figure 20 and Figure 21, respectively. The exhaust temperature ramp-up period was generally slower than the metal piston for all coated pistons except the 200-micron GZO piston. However, the final exhaust temperature at the end of the test was only 1 K higher for the 200-micron GZO piston versus the metal baseline. There was a 15 K difference in exhaust temperature between the 200-micron NC w/ CCC piston and metal baseline. The exhaust temperature results tend to agree with those recorded during the steady state testing. The unburned hydrocarbon emissions were generally reduced with a coating, which agrees with other results in the literature [66]. Except for the 200-micron NC piston, the peak in unburned hydrocarbon emissions was lower and the final point was generally lower than the metal baseline. The 200-micron NC piston produced more unburned hydrocarbon emissions than the metal piston, but this is believed to be an outlier because the equivalence ratio was not as well controlled as the other coated pistons. Except for the 200-micron piston, the trends in unburned hydrocarbon emissions agree with the PM emission results in which the most significant changes occurred with thicker pistons that encountered a charge heating effect. The unburned hydrocarbon emissions for the individual cold-start tests for each piston are presented in APPENDIX B.

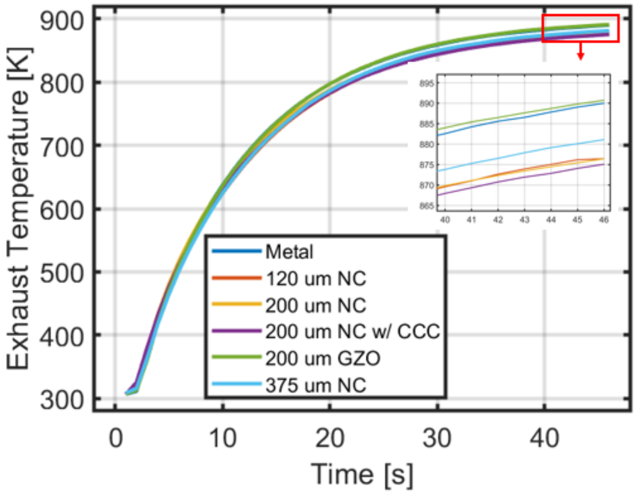

Figure 20: Average exhaust temperature during cold-start tests.

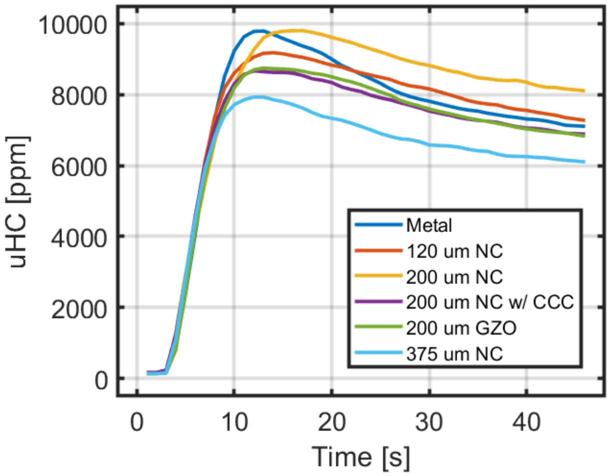

Figure 21: Average unburned hydrocarbons during cold-start tests.

3.5 Discussion

The experiments presented thus far have showed that the novel NC material must be applied as a thin coating to maximize its benefits in the combustion chamber. Increased knock propensity in SI with TBCs is the result of two factors:

1. Open cycle charge heating elevating the IVC temperature of the incoming charge.

2. Closed cycle heat transfer reduction during compression and combustion.

Both effects increase the pressure and temperature in the end-gas, increasing knock propensity. The first factor can be addressed by using thin, low thermal inertia coatings such as the 120-micron NC piston. However, the closed cycle heat transfer reduction is more difficult to address since the heat transfer reduction is the mechanism to increase efficiency with TBCs in SI engines. A sufficient amount of open cycle cooling is necessary to counteract the knock penalty induced by closed cycle heat transfer reduction. This was observed with the 120-micron NC, 200-micron NC w/ CCC, and 200-micron GZO pistons. From a cold-start perspective, thicker coatings produced favorable results, but this was accompanied by significant knock penalties under steady-state conditions.

TBCs with thicknesses close to the material's penetrative depth produced favorable results. At 1500 RPM, the NC material has a penetrative depth of ~120-microns. Assuming the bond coat was evenly applied at 50-microns across all pistons, the NC material thicknesses on the 120-micron NC piston was 70-microns total, and thus generated the largest spark advance among all pistons tested because the coating was too thin to store heat. However, because the thickness was well below the penetrative depth, the surface temperature swing of the coating was not maximized. Increasing the thickness to 200-microns and above was detrimental to efficiency and knock intensity as the coatings stored excessive amounts of heat with no corresponding increase in temperature swing. Thus, it is more favorable to apply a coating that is too thin than too thick.

The application of the CCC topcoat allowed some performance recovery by virtue of lowering the thermal inertia of the composite coating. The CCC topcoat itself has a penetrative depth of ~100-microns at 1500 RPM, and it is assumed that the penetrative depth of the composite TBC (NC + CCC) is lower than NC by itself. With a lower penetrative depth and nearly equal thickness to the 200-micron NC piston according to Table 4, it would have been expected that the CCC topcoat would elicit a knock penalty from charge heating similar to the 200-micron coating with no topcoat, but the opposite was shown. Currently, there is no explanation for why, although the uncertainty in the thickness measurement of the 200-micron NC w/ CCC piston in Table 4 calls into question if the alkali binder in the CCC material was interfering in the measurements. The alkali binder that was used was composed of lithium polyciliate, which is a salt composed of negatively charge silicate and positively charger lithium. It is possible this ionic compound can interfere with the eddy current measurements from the Dualscope ETA3.3H probe. Thus, the thickness of the 200-micron NC w/ CCC piston could have been overestimated and the true thickness is most likely lower. Further work should focus on the impact of topcoat materials, either for sealing or catalytic purposes, on these low thermal inertia TBCs.

The penetrative depth of GZO is ~125-microns at 1500 RPM based on the material properties listed in Table 5, thus the 200-micron GZO piston exceeded its penetrative depth by ~20-microns. However, the variability in measured conductivity throughout the literature [46] implies that a range of ~100-microns to ~145-microns are possible penetrative depths. Based on the experimental results, it can be inferred that the true penetrative depth of GZO was closer to the latter. The 200-micron GZO piston demonstrated a maximum net thermal efficiency gain of 0.16% ± 0.42%, whereas the 120-micron NC piston achieved a maximum gain of 0.30% ± 0.44%.

It can be concluded that thin TBCs can take advantage of both heat transfer reduction and KLSA extension in SI engines. However, thicker TBCs produced more favorable cold-start performance from an emissions perspective. The 200-micron GZO piston was capable of compromising between steady state and cold-start regimes, but the efficiency gains remain rather small and can be characterized by experimental uncertainty. From a materials science perspective, research is ongoing with regards to improving thermophysical properties of these coatings.

Overall, this chapter provided insight into the challenges of TBCs in SI. Thin coatings can take advantage of both heat transfer reducing and KLSA extension during steady state conditions. Thicker coatings produced larger emissions during cold-start tests. Favorable performance between both operating regimes was demonstrated with the 200-micron GZO piston, which showed notable reductions in cold-start emissions with a slight KLSA advance at steady-state conditions, but the 120-micron NC piston encountered the largest net thermal efficiency gains under steady conditions.

CHAPTER 4. IMPACT OF COATED VALVES

It has been established that small, but non-negligible efficiency increases are possible with thin, low thermal inertia TBCs on the piston. However, the net thermal efficiency changes across all tested pistons can be characterized by the experimental uncertainty. To enable larger efficiency changes, either additional charge cooling measures must be established to enable more spark advance or more surfaces must be coated with TBCs. In both cases, the intake and exhaust valves are ideal components to coat since they contribute significantly to closed cycle surface area and interact with the air during gas exchange. This chapter will study the contribution of intake and exhaust valves with the backside and combustion faces coated (see Figure 4) and determine the contribution of each coated valve. Four different coating configurations are listed in Table 10. The coated piston was the 120-micron NC piston, which has already been characterized in the previous chapter. Between tests, CCD growth was removed from the coating surfaces with oven cleaner.

Table 10: Testing configuration labels with coated components listed.

Configuration Label	**Coated Piston**	**Coated Intake Valve**	**Coated Exhaust Valve**
Metal	X	X	X
All Coated	✓	✓	✓
IV Only	✓	✓	X
EV Only	✓	X	✓

4.1 Coated Valves: Speed Sweep

Net thermal efficiency, knock intensity, and exhaust temperatures at 1200 RPM, 1800 RPM, and 2200 RPM are shown in Figure 22. The largest improvement in net thermal efficiency was recorded when the coated surface area was maximized. Previously, the 120-micron NC piston produced a slight KLSA advance of 1.5 degrees relative to is metal baseline (at 1200 RPM, 8 bar IMEP_n in Figure 16). The addition of coated valves in this study erased the spark advance as the CA50 was approximately even between the baseline and fully coated configuration. The absence of a large knock penalty relative to the metal baseline in the fully coated configuration implies that open cycle charge cooling countered knock derived from heat transfer reduction.

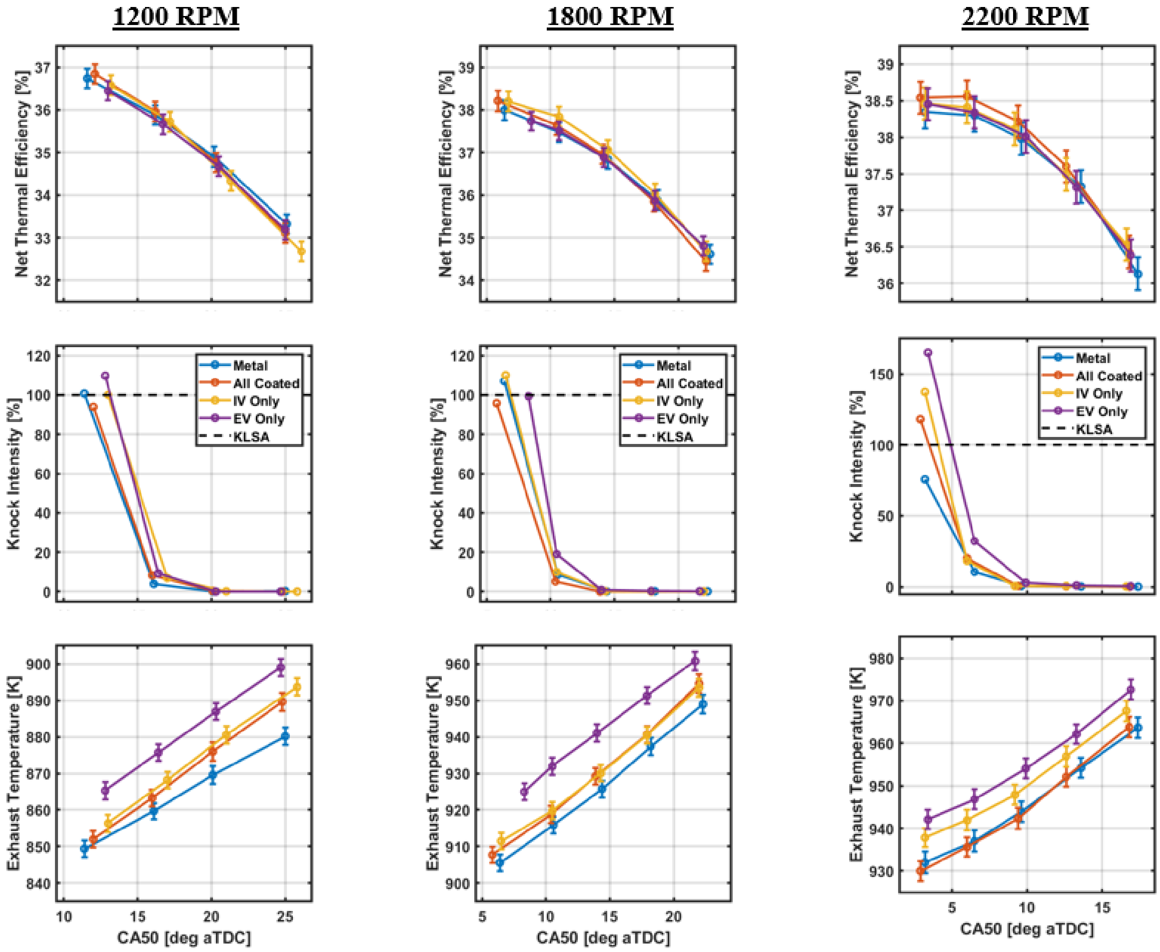

Figure 22: CA50 vs. net thermal efficiency, knock intensity, and exhaust temperature of coated valve configurations at 1200 RPM, 1800 RPM, and 2200 RPM at 8 bar IMEP$_n$. The black dashed line represents the KLSA.

Staged removal of each set of coated valves showed mixed performance results. Notably, the absence of the coated intake valve generated a knock penalty in the exhaust valve only configuration (labelled EV Only) at both 1800 RPM and 2200 RPM. At equivalent spark timings, the coated exhaust valve configuration either matches or slightly exceeds the net thermal efficiency of the metal reference, and the higher exhaust temperatures suggest that a heat transfer reduction was achieved. However, the knock intensity limit was regularly exceeded at advanced spark timings with the coated exhaust valve configuration, further limiting efficiency gains across the spark timing sweeps. Contrary to the exhaust valve arrangement, there was a less severe knock penalty with coated intake valve configuration (labelled IV Only), which allowed spark advance similar to the metal reference. The exhaust temperature of the coated intake valve configuration generally matched the fully coated configuration, which indicates that the coated exhaust valve was largely responsible for higher exhaust temperatures in the individual coated valve arrangements.

In the fully coated configuration, knock intensity closely aligns with the metal baseline at 1200 RPM and 1800 RPM. At 1200 RPM, the CA50 was retarded by 0.5 degrees, and at 1800 RPM was advanced by 0.5 degrees. At 2200 RPM, however, the knock intensity clearly exceeds the metal baseline and the 100% knock limit, indicating that the coatings are experiencing a bulk shift in surface temperature rather than a dynamic temperature swing. At higher speeds, the penetrative depth decreases since heat transfer is time-based and the temperature swing magnitude declines. Thus, the coatings are likely to retain more heat at higher speeds. Interestingly, the fully coated configuration did not experience the largest knock penalty at 2200 RPM despite having the most coated surface area. Instead, the coated exhaust valve configuration had the largest knock penalty, with the coated intake valve configuration falling in between the fully coated and coated exhaust valve configuration.

4.2 Coated Valves: Load Sweep

Net thermal efficiency, knock intensity, and combustion efficiency versus CA50 for the 4 bar, 8 bar and 12 bar $IMEP_n$ operating conditions are shown in. The 4 bar $IMEP_n$ operating condition does not have the knock intensity plot because it was not knock limited. The spark timing sweep at 4 bar $IMEP_n$ started at a spark timing of -15 degrees aTDC and was advanced until -33 degrees aTDC. At retarded spark timings in the beginning of the sweep, the CA50 of the fully coated configuration was significantly advanced compared to the metal reference. As the spark timing advanced, the CA50 difference between the metal and fully coated configuration diminished. The fully coated configuration produced a net thermal efficiency increase of 0.31% ± 0.72%. The coated intake valve only configuration achieved a net thermal efficiency increase of 0.34% ± 0.74%, and the coated exhaust valve only configuration failed to achieve any efficiency benefit. With the 120-micron NC piston by itself, a net thermal efficiency increase of 0.24% ± 0.68% was recorded in Figure 17. The extent of the performance degradation of the coated exhaust valve configuration was realized at 12 bar $IMEP_n$. Like the speed sweep, a slight efficiency benefit was realized at advanced, non-knock limited spark timings, but the knock penalty at KLSA limited further efficiency gains. At 12 bar $IMEP_n$, this translated to a ~0.70 percentage point decrease in net thermal efficiency.

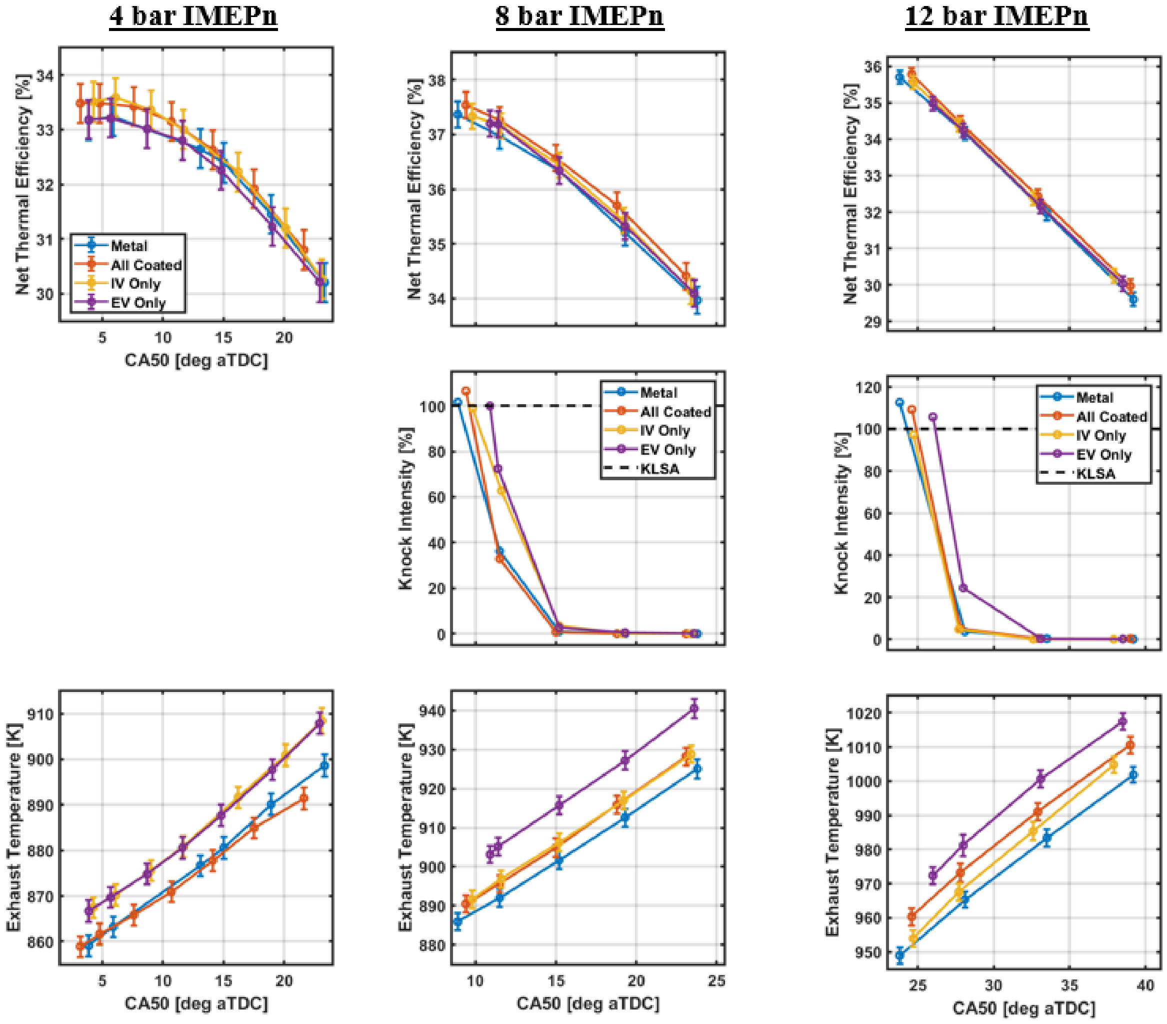

Figure 23: Net thermal efficiency, knock intensity, and combustion efficiency of the coated valve configurations at 4 bar, 8 bar, and 12 bar IMEP$_n$ at an engine speed of 1500 RPM. The black dashed line represents the KLSA limit. Note that 4 bar IMEP$_n$ does not have knock intensity because that operating condition was not knock limited.

Table 10 presents a summary of the absolute efficiency changes at each coating configuration's KLSA with respect to the corresponding metal baseline. Uncertainty bands are not provided for presentation purposes, but are in the range of ± 0.75% at 4 bar IMEP$_n$, ± 0.42% at 8 bar IMEP$_n$, and ± 0.36% at 12 bar IMEP$_n$. The addition of coated intake and exhaust valves generated the largest efficiency gain relative to the coated piston individually. Application of the coated exhaust valve by itself generated consistent efficiency losses derived from retarded KLSA.

When knock was not a consideration, the coated exhaust valve configuration generated very slight increases in net thermal efficiency but was still lower than the coated piston by itself. On an individual basis, the coated intake valve configuration demonstrated superior performance, but still lagged slightly when both valves were installed. Overall, this suggests that the benefits and drawbacks of each coated valve were not additive when combined.

Table 11: Absolute net thermal efficiency gain for the coated piston, coated piston with coated exhaust valve, coated piston with coated intake valve, and coated piston with both coated valves at KLSA with respect to each configuration's uncoated baseline.

	Coated Piston Only	**Coated Exhaust Valve + Coated Piston**	**Coated Intake Valve + Coated Piston**	**Fully Coated**
1200 RPM, 8 bar IMEP$_n$	0.30	-0.29	-0.16	0.10
1500 RPM, 4 bar IMEP$_n$	0.24	0.01	0.34	0.31
1500 RPM, 8 bar IMEP$_n$	0.08	-0.16	-0.03	0.18
1500 RPM, 12 bar IMEP$_n$	0.10	-0.72	-0.15	0.18
1800 RPM, 8 bar IMEP$_n$	0.07	-0.25	0.21	0.22
2200 RPM, 8 bar IMEP$_n$	0.15	0.10	0.12	0.22

Table 12 shows the difference in spark timing at each configuration's KLSA with respect to the metal baseline KLSA at the knock-limiting operating conditions. Negative numbers indicate a spark timing retard, whereas positive values indicate spark timing advances. The coated piston by itself generates its efficiency gains through spark advance because of open cycle charge cooling. The addition of coated valves, however, caused either no spark timing change or a spark timing retard. Since the fully coated configuration did not derive an efficiency gain from a significant KLSA change, it can be assumed that most of the change in net thermal efficiency was a product of blocked heat transfer rather than open cycle charge cooling.

Table 12: Spark timing degree difference between each coating configuration's KLSA with respect to their own uncoated baseline. Negative numbers indicate a spark timing retard, and positive numbers indicate a spark timing advance.

	Coated Piston Only	**Coated Exhaust Valve + Coated Piston**	**Coated Intake Valve + Coated Piston**	**Fully Coated**
1200 RPM, 8 bar IMEP$_n$	1.5 degrees	-0.6 degrees	0.0 degrees	0.0 degrees
1500 RPM, 8 bar IMEP$_n$	1.3 degrees	-1.8 degrees	-0.8 degrees	-0.8 degrees
1500 RPM, 12 bar IMEP$_n$	0.5 degrees	-1.5 degrees	-0.8 degrees	-0.8 degrees
1800 RPM, 8 bar IMEP$_n$	0.5 degrees	-2.0 degrees	-0.2 degrees	0.2 degrees

4.3 Discussion

As it stands, each coating configuration offers a different set of benefits. The coated exhaust valve configuration experienced a retarded KLSA, countering efficiency gains at individual spark timings at knock-limited conditions. However, the coated exhaust valve generated the highest exhaust temperatures across all operating conditions, which is beneficial for turbocharging and aftertreatment. The coated intake valve encountered a less severe KLSA retard, but efficiency gains were limited to three out of the six operating conditions in Table 11. The increase in exhaust temperature in the coated intake valve configuration was not as high as the exhaust valve only configuration. However, the behavior of the two valves when installed together were not additive. The fully coated configuration featured a knock penalty and exhaust temperature increase on the order of the intake valve only configuration, but generated an efficiency gain larger than both individual valves, likely due to the higher fraction of coated surface area in the combustion chamber.

It is unclear why the behavior of each individual coated valve was not additive when installed together. One obvious explanation for the mismatch between individual valve configurations and the fully coated configuration is the change in discharge coefficient during gas exchange. The combination of thickness and roughness on the valve backside can potentially impact flow separation and motion during the intake and exhaust strokes. Similarly, the additional thickness on the valve faces and backsides can effectively reduce the lift of the valve and change the residual fraction or inlet conditions. Finally, there is the potential of fuel absorption in the backside coatings during injection. The injection occurs early in the intake stroke while the intake valve is opening. During an engine tear down, there was visual evidence of fuel impingement on the backside of an intake valve, which is shown in Figure 24. Fuel absorption on the coated piston in the form of increased unburned hydrocarbons was not observed in these studies due to the low injection pressure (100 bar), early injection timing, and low porosity coating (less than 10%), but other authors have reported such behavior [23]. A well validated CFD model would be necessary to evaluate these theories.

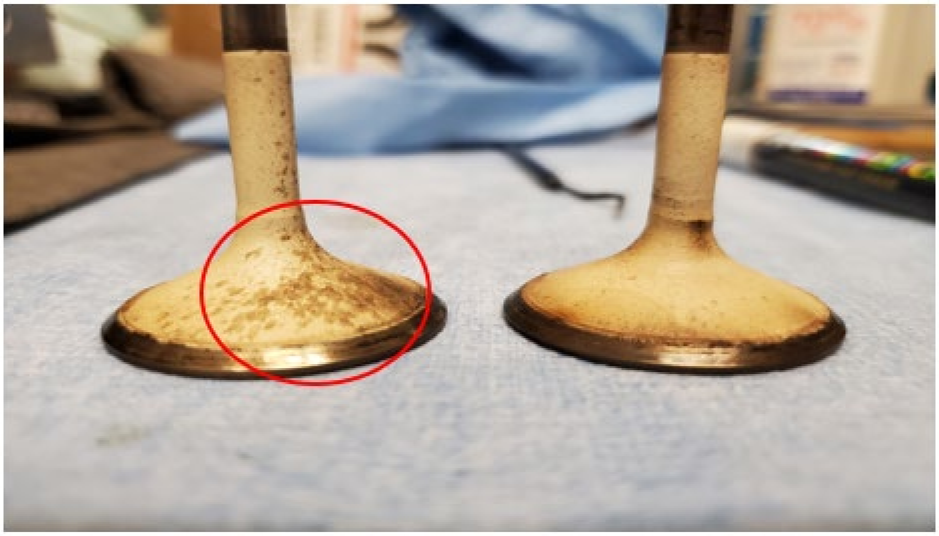

Figure 24: Fuel impingement on the backside of an intake valve (circled in red).

It can be inferred from this study that the coated intake valve has outsized importance over the coated exhaust valve. Individually, the knock penalty reduction from the coated exhaust valve to the coated intake valve was likely derived from the coated backside on the intake valve. The purpose of the coated backsides and stems on the intake valves was to block heat transfer from the combustion chamber from escaping into the air sitting on the valve during the closed cycle. Similarly, the coated backsides on the exhaust valves were aimed at preventing heat transfer from the escaping gases into the exhaust valve, thus lowering the component temperature and increasing the exhaust gas temperature. The sensitivity of knock due to elevated exhaust valve surface temperature has been well documents. A 3D CFD study performed by Robert et al. demonstrated the tendency of end-gas auto-ignition to occur near the exhaust valve [67]. An experimental study done by Merola and Vaglieco on an optically accessible engine measured a large concentration of radical species (OH and HCO) critical to auto-ignition and knock near the exhaust valves [68]. This study suggests that the coated backsides of the intake valve prevented excessive charge heating and the coated backsides of the exhaust valve failed to lower the component temperature.

Of course, the presence of a coated backside and combustion face opens the possibility of several coating combinations. The optimal coating configuration most likely requires a coated intake valve, but it is an open question as to whether a fully coated exhaust valve is required. In this study, both valves were sprayed with GZO to the same thickness. Thicknesses above the penetrative depth of the material will not increase the surface temperature swing, instead storing heat and promoting charge heating, whereas thicknesses less than the penetrative depth fail to maximize the surface temperature swing. Because of the exhaust valve's propensity to induce knock, a coating significantly less than the penetrative depth should be applied on the combustion face since the downside of a lower temperature swing is far more advantageous than the downside of increased knock propensity. However, the intake valve combustion face could be coated to a thickness close to the penetrative depth since heat transfer is unidirectional towards the port where fresh air enters the cylinder. The backsides of both valves can be coated as thick as possible without concern of charge heating since the goal would be to block as much heat from entering the valve. In the case of the intake valve, blocking heat transfer to the air sitting on the backside of the valves would reduce the gas' IVC temperature, whereas the exhaust valve backside will increase exhaust temperature through minimizing heat escaping into the valve.

Simulated cold-starts were not performed in this experimental campaign since the purpose of these experiments was to develop a coating configuration for a 2021 Ford 2.3 Liter Ecoboost multi-cylinder engine. In theory, the addition of coated surface on the valves and cylinder head will provide an improvement in emissions and exhaust temperature. On a production engine, the data collected will be more relevant compared to those collected on the single-cylinder research engine.

Another interesting result from this study was the relatively low net thermal efficiency change from the addition of coated valves compared to the coated piston. In Table 11, the efficiency change from the addition of coated valves relative to the coated piston was only ~0.05 percentage points on average. Overall, the maximum possible efficiency change was ~0.30 percentage points without the head coated, which was not possible for this single-cylinder research engine. Thermodynamic analysis of low thermal inertia coatings was performed in parallel to the studies presented in this thesis in order to understand the fundamental limitations of TBCs in SI [57]. Even without the consideration of knock in the model, the study confirmed the experimental results showing the efficiency increases are rather small. This is shown in Figure 25, which shows the net fuel conversion efficiency vs. CA50 of various thicknesses of the NC coating on the piston, head, and valve faces at the 1500 RPM, 8 bar $IMEP_n$ operating condition. In this thesis, the results between net thermal and net fuel conversion efficiency followed the same trends across all coating configurations. The maximum change in efficiency was ~0.25 percentage points.

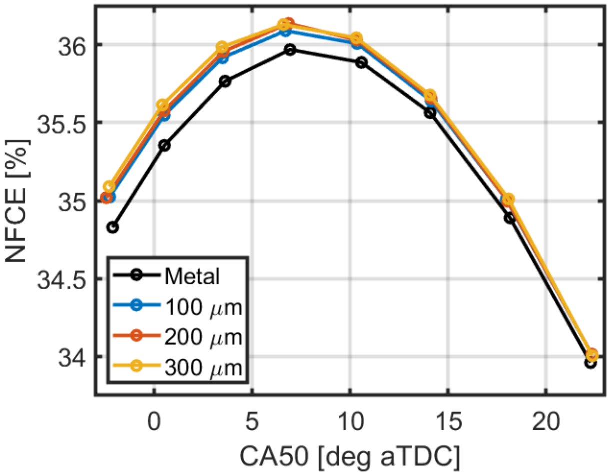

Figure 25: Net fuel conversion efficiency (NFCE) vs. CA50 at 1500 RPM, 8 bar IMEP$_n$ for the baseline metal piston and 100-, 200-, and 300-micron NC coating applied on the piston, head and valve faces [57].

Artificially deactivating heat transfer for 10 crank angle degrees in the model further increased the net fuel conversion efficiency by 0.95 percentage points. As evidenced by the experimental results, a spark retard due to increased knock propensity can significantly reduce or eliminate this efficiency increase. Furthermore, some of the natural disadvantages of SI make it difficult to extract meaningful efficiency increases through heat transfer reduction. Increasing the compression ratio of the engine from 9.3 to 16 increased the net fuel conversion efficiency by 2.0 percentage points. In practice, a compression ratio of 16 is too high to run gasoline in SI engines. Additionally, a surface temperature swing of ~100 K in stoichiometric operation where the gas temperatures are high (~2600 K) is a relatively small reduction in temperature difference. This is shown in Figure 26, which shows the temperature difference between the gas temperature and the surface temperature of a 300-micron NC piston. Even though these factors limit the efficiency increase associated with blocking heat transfer in SI, optimizing the coating material, coating thickness, and location can still provide a modest and non-negligible benefit to efficiency, knock and cold-start performance.

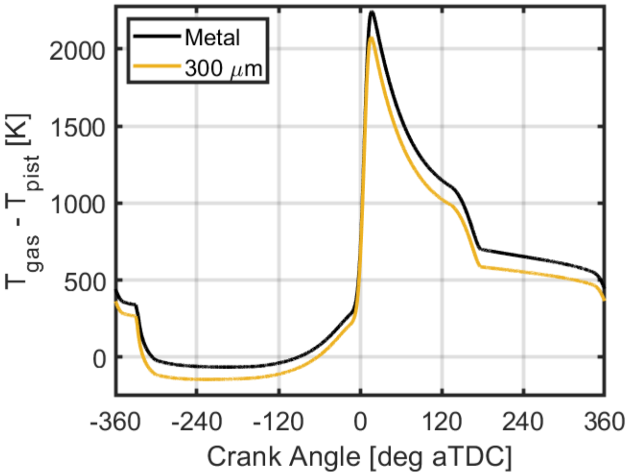

Figure 26: Gas temperature minus piston surface temperature vs. crank angles for the metal baseline and for a 300-micron NC coating applied to the piston, head, and valves [57].

CHAPTER 5: ANALYSIS OF CCD GROWTH ON TBCS

The final topic of this thesis will analyze the effect of CCD growth on TBCs. As previously mentioned, CCDs behave similarly to TBCs and will grow and decay throughout engine operation. Thus, it is important to analyze the impact of these naturally grown deposits when considering TBCs as a part of the overall engine system.

5.1 Thickness Measurements

A 130-micron NC coated heat flux probe was installed in the cylinder head with a 200-micron NC coated piston. Over a period of 62.5 hours, CCD was grown on both the coated heat flux probe and the coated piston. The thickness of the CCD layer on the coated heat flux probe is shown in Table 13. The CCD layer on the coated heat flux probe reached an equilibrium thickness of 28.8 microns after 62.5 hours. After 3 hours of running at a high load and speed operating condition, the CCD thickness was measured at 10.2 microns, effectively erasing 50 hours of growth in a 3-hour period. At the end of the test, the CCD layer was wiped off the probe and the measured thickness statistically matched the baseline TBC thickness. Since the measuring probe diameter was larger than the sample surface, the uncertainty was large. Additionally, only a thin layer of CCD was grown on the heat flux probe. The heat flux probe was slightly recessed in the cylinder. In a similar study, Hoffman et al. captured approximately 25-microns of CCD growth in HCCI on a heat flux probe coated with magnesium zirconate after 40-hours of running [69].

Table 13: Coated heat flux probe thickness after CCD accumulation (0 hours to 62.5 hours), CCD burn-off (Post-burn-off) and thickness after wiping the coated heat flux probe clean of CCD.

	Thickness [µm]
Baseline – 0 hours	130.0 ± 6.1

12.5 hours	140.5 ± 22.9
25 hours	149.1 ± 5.6
37.5 hours	152.9 ± 7.2
50 hours	158.0 ± 2.7
62.5 hours	158.8 ± 9.2
Post burn-off	140.2 ± 4.6
Wiped CCD	131.3 ± 15.3

Thickness measurements on the piston crown are shown in Figure 27. Measurements were recorded after 62.5 hours and after the burn-off phase. Note that these measurements include the TBC layer below the CCD. As opposed to the coated heat flux probe, there was significant deposition, with some areas measuring over 200-microns of CCD growth on the TBC surface. Significant variation exists between different locations, with the exhaust side of the piston exhibiting thicker CCDs than the intake side. Fuel was delivered in a centrally mounted direct injector, but incoming intake air motion likely caused the fuel spray to impinge more fuel on the exhaust side of the piston, creating an uneven distribution of CCDs on the piston surface.

Location	Total Thickness – 62.5 hours [µm]	Total Thickness – Burn-off [µm]
A	259.1 ± 26.4	247.4 ± 13.3
B	360.7 ± 22.5	342.9 ± 21.5
C	543.6 ± 31.5	439.4 ± 17.3
D	431.8 ± 19.5	408.9 ± 59.0
E	464.8 ± 53.5	388.6 ± 69.0
F	387.5 ± 29.9	335.3 ± 5.8
G	442.0 ± 64.0	327.7 ± 86.8
H	434.3 ± 15.4	378.5 ± 4.4
I	269.2 ± 20.8	261.6 ± 24.4
J	225.0 ± 5.1	221.0 ± 4.1
K	225.6 ± 3.2	221.5 ± 4.2
L	289.6 ± 19.5	254.0 ± 5.2

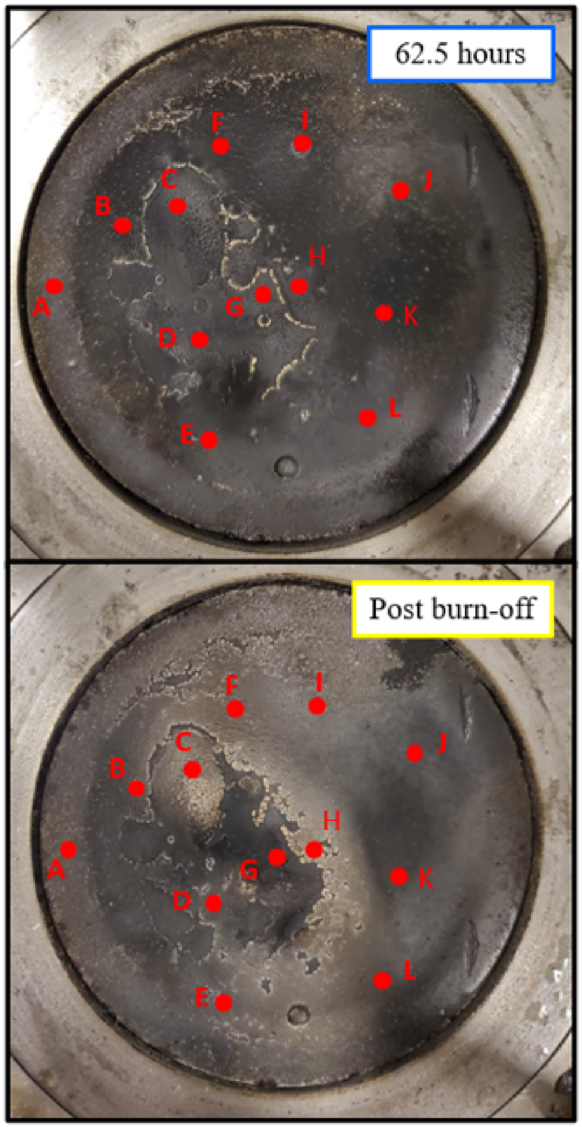

Figure 27: Coated piston thickness measurements with marked locations after CCD accumulation and burn-off phases. The exhaust side of the piston is the left side and the intake side is the right side.

The burn-off period removed CCDs from the TBC surface, but some areas retained relatively large thicknesses. Additionally, there was no observable pattern with regard to which section of the piston experienced the largest removal of CCD. To verify the adhesion of the CCDs to the piston surface, oven cleaner was used to forcibly clean the surface until the TBC was visible.

Even though the original TBC surface of the piston was exposed on the intake side of the piston right side, the exhaust side could not be completely cleaned as shown in Figure 28. A final note regarding the piston crown images in Figure 27 and Figure 28 is that two dents are visible on the intake side of the piston (right side). Those dents were created during an engine rebuild that predated the start of this study where the timing belt was improperly timed, causing the valves to contact the piston surface. Despite this, the TBC did not show any evidence of failure near the dents or anywhere else on the surface.

Figure 28: Coated piston before the durability test (left image) and coated piston after the durability test with CCDs forcibly removed. The exhaust side of the piston is the left side and the intake side is the right side.

5.2 Conductivity Measurements

Conductivity values for the composite TBC/CCD layer on the coated heat flux probe are presented in Table 14. Conductivity decreased until a steady state was reached after 25 hours of CCD growth (CCD thickness was 20-microns). As previously mentioned, the uncertainty was large because the temperatures across the heat flux probe were small. The decrease in conductivity uncertainty generally aligns with Figure 9, where the increase in coating surface and backside temperature difference decreased both the conductivity and its uncertainty. After completing the burn-off phase, the CCD layer was wiped from the coated heat flux probe and conductivity was measured again to verify if the TBC conductivity returned to its initial value. The final conductivity of ~1.21 was close to the initial ~1.31, but it is possible that CCD growth within the pores of the coating could have affected the measurement.

Table 14: Conductivity measurements of the coated heat flux probe during CCD accumulation (0 to 62.5 hours), CCD burn-off (Post burn-off), and after wiping the coated heat flux probe of CCD (Wiped CCD)

	Conductivity [W/m/K]
Baseline – 0 hours	1.3051 ± 1.6472
12.5 hours	1.1466 ± 0.9974
25 hours	0.9010 ± 0.9894
37.5 hours	0.8606 ± 0.5360
50 hours	0.9233 ± 0.5830
62.5 hours	0.9542 ± 0.7408
Post burn-off	1.0569 ± 0.7408
Wiped CCD	1.2080 ± 0.9232

With the baseline TBC and overall coating system conductivity known, the standalone CCD conductivity can be calculated through a thermal resistance calculation [70]. Assuming a uniform two-layer system, the CCD conductivity can be expressed as:

$$k_{CCD} = \frac{x_{CCD}}{\frac{x_{tot}}{k_{tot}} - \frac{x_{TBC}}{k_{TBC}} - R_c} \tag{11}$$

where R_c is the contact resistance between the TBC and CCD layer, x_{CCD}, x_{TBC}, and x_{tot} are the thicknesses of the CCD, TBC, and total system, respectively, and k_{CCD}, k_{TBC}, and k_{tot} are the conductivity of the CCD, TBC, and total system, respectively. The contact resistance term compensates for interfacial features between the CCD and TBC layer, such as the open pores, but is difficult to estimate. Assuming there was no contact resistance for simplicity, the CCD conductivity from 12.5 hours to the post burn-off period is shown in Table 15, with the average conductivity coming out to 0.3626 W/m/K. Despite the uncertainties in the measurement process and assumption of no contact resistance, this value agrees with those presented in other works [37], [38]. The calculations suggest that CCDs are superior insulators compared to manufactured TBC since the CCD layer only contributes 18% of the total system thickness but yields 40% of the total thermal resistance. Conductivity has an outsized important in determining TBC effectiveness [18]. The difficultly with considering CCDs as effective TBCs is that CCD growth is highly varied in magnitude, and as the accumulation and burn-off phases demonstrated, significant amounts of CCD can be grown and removed quite rapidly.

Table 15: CCD conductivity calculated through Equation (11), assuming negligible contact resistance between TBC and CCD layers.

	Conductivity [W/m/K]	**Contribution to Total Thermal Resistance [%]**
12.5 hours	0.4580	18.7
25 hours	0.2899	39.8
37.5 hours	0.2934	43.9
50 hours	0.3915	41.8

62.5 hours	0.4311	40.2
Post burn-off	0.3087	24.9

5.3 Diffusivity Measurements

Diffusivity of the composite TBC/CCD layer of the coated heat flux probe is shown in Table 16. Outside of the error bounds, the first 25 hours of CCD growth showed no statistically significant variation in diffusivity during the first 20-microns of deposition. Hoffman also experienced these inconclusive trends with low thickness CCD on a clean metal heat flux probe in HCCI, but the diffusivity trends stabilized once the CCD thickness exceeded 30-microns [71]. This was attributed to the non-uniform nature of CCD growth on the surface of the heat flux probe, with potential pores and gaps allowing some radiation to directly hit the surface of the heat flux probe as opposed to travelling through a uniform layer of coating. Thus, non-uniformities along the surface of the heat flux probe could have caused this behavior. After 25 hours, the diffusivity consistently decreased as CCD thickness increased, but the overall change was small. Similar to the conductivity measurements, the diffusivity was measured after completely wiping the coated heat flux probe clean of CCD and the final measurement closely matched the baseline measurement.

Table 16: Diffusivity measurements of the coated heat flux probe during CCD accumulation (0 to 62.5 hours), CCD burn-off (Post burn-off), and after wiping the coated heat flux probe of CCD (Wiped CCD).

	Diffusivity [mm^2/s]
Baseline – 0 hours	0.2101 ± 0.0216
12.5 hours	0.1865 ± 0.0595

25 hours	0.2299 ± 0.0193
37.5 hours	0.1972 ± 0.0193
50 hours	0.1770 ± 0.0078
62.5 hours	0.1610 ± 0.0187
Post burn-off	0.2220 ± 0.0169
Wiped CCD	0.2135 ± 0.0494

The phase lag between the clean metal and coated heat flux probes are shown in Figure 29. The motor speed refers to the speed at which the slotted chopping wheel was driven. The phase lag between the uncoated and coated heat flux probes follows the same trend as diffusivity where phase lag does not significantly change after 20-micron of CCD growth. After 20-microns of CCD growth, the phase lag clearly increased as additional layers of CCD slowed the temperature response of the coating backside temperature junction. This trend was consistent across the three motor speeds.

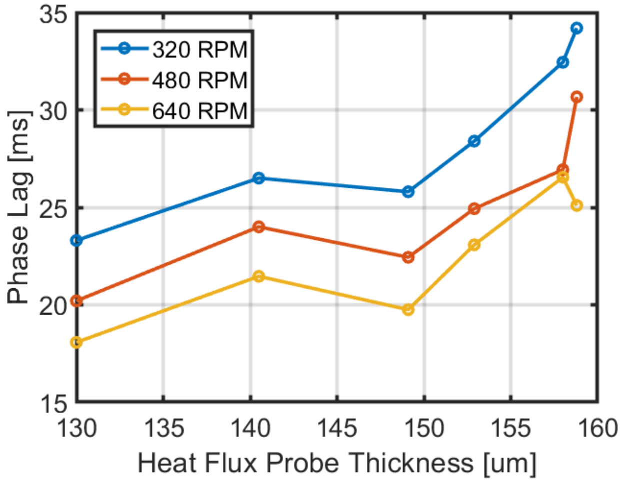

Figure 29: Phase lag vs. coated heat flux probe thickness between the clean and coated heat flux probes across multiple motor speeds.

Figure 30 shows the normalized temperature swing of the coating backside temperature at a motor speed of 480 RPM across multiple CCD thicknesses. The peak temperature swing slightly decreased as CCD thickness increased. Additionally, the temperature swing appeared slightly elongated with increasing CCD thickness, indicating that there was some heat storage in the coating. However, if the system thickness was exceeding the penetrative depth, the coating backside temperature would show no temperature swing. When taken together with the conductivity measurements, these results indicate that the TBC/CCD layer was not storing a significant amount of additional heat.

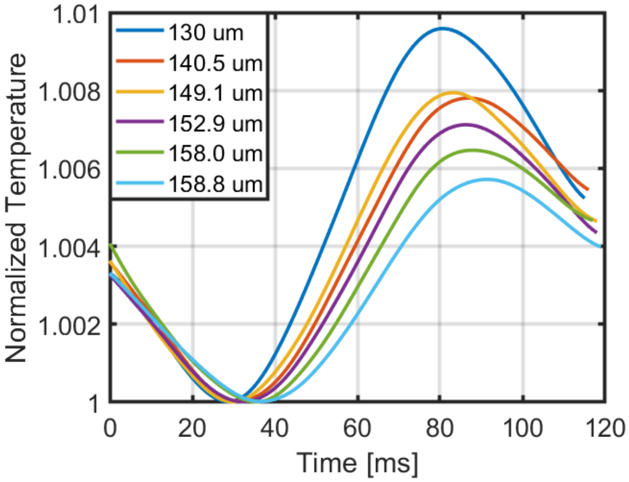

Figure 30: Normalized subsurface temperature of the coated heat flux probe with different thicknesses of CCD at a motor speed of 480 RPM.

5.4 Engine Performance

A total of seven spark timing sweeps were performed. The air and fuel mass were kept constant and stoichiometric to achieve an initial load of 7.5 IMEP$_g$ (gross indicated mean effective pressure) at an initial spark timing of -9 degrees aTDC. Since the air flow controller maintained the same flow rate through changes in intake pressure, charge heating could be observed by analyzing the intake pressure trace in Figure 31. The first change in intake pressure was 1.5 kPa increase after

12.5 hours, followed by statistically insignificant changes characterized by uncertainty. The overall increase in intake pressure to maintain the same air flow rate indicated hotter combustion chamber surfaces and charge heating. While there was no CCD thickness measurements for the piston crown at each time interval, these results indicate that a significant portion of the CCD buildup occurred within the first few hours of running.

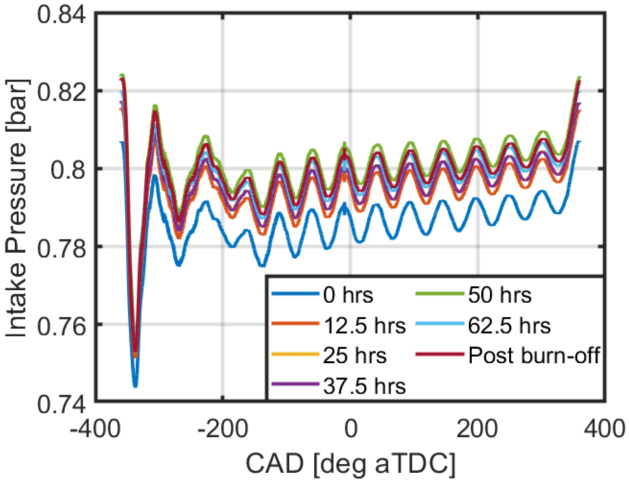

Figure 31: Average intake pressure vs. crank angle at an initial spark timing of -9 degrees aTDC during CCD accumulation (0 hours to 62.5 hours) and CCD burn-off (Post-burn-off).

Exhaust temperature and knock intensity vs. CA50 are presented in Figure 32. The growth of CCDs resulted in hotter exhaust temperature and increased knock propensity. For each spark timing sweep, the first three spark timings are the same (-9, -12, and -15 degrees aTDC), with the earliest spark timing (indicated by the most advanced CA50 in that sweep) representing the KLSA. The knock limited CA50 was retarded by CCD growth, with a 4.2-degree shift in spark timing from 0 hours to 62.5 hours. Interestingly, the burn-off phase almost returns the exhaust temperature and knock intensity to the 12.5-hour mark, with the coated heat flux probe thickness at those two points almost matching according to Table 13.

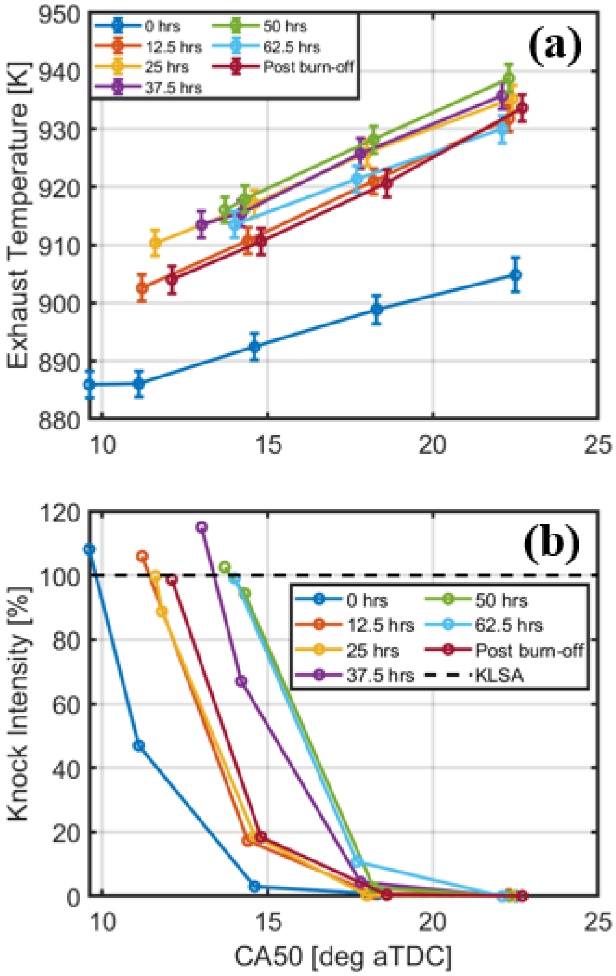

Figure 32: CA50 vs. (a) exhaust temperature and (b) knock intensity during CCD accumulation (0 hours to 62.5 hours) and CCD burn-off (Post-burn-off).

The retarded knock limited CA50 with increased CCD growth was expected since such behavior has been previously reported in the literature [35]. The higher exhaust temperature also suggests that the CCD layer was behaving similarly to a traditional, thick insulator prone to storing excessive heat. Although the operating conditions in this study and Chapter 3 were slightly different, it was hypothesized that the consistent decline in exhaust temperature with a low thermal inertia coating was because the transient nature of the surface temperature was not capable of effectively increasing the exhaust gas temperature. By that logic, the higher exhaust temperatures seen CCD deposition in this study indicates that the surface temperature was transitioning from a dynamic temperature swing to a bulk temperature increased through increased charge heating. Evidence from Figure 30, while small, suggests that the subsurface temperature swing was dampening with thicker CCD, which is consistent with a material approaching its penetrative depth.

Net thermal efficiency across all seven spark timing sweeps is shown in Figure 33. Net thermal efficiency at KLSA is shown in Figure 34. The first 12.5 hours of CCD growth produced the largest increase in efficiency, but further growth maintains a constant efficiency between the baseline and 12.5-mark. The net thermal efficiency at KLSA declined as the spark timing was retarded to maintain the knock intensity at 100%. After the burn-off phase, the efficiency did not return to the equivalent heat flux probe thickness at 12.5-hours like knock intensity and exhaust temperature in Figure 32, but did increase relative to the 62.5-hour mark before the burn-off phase.

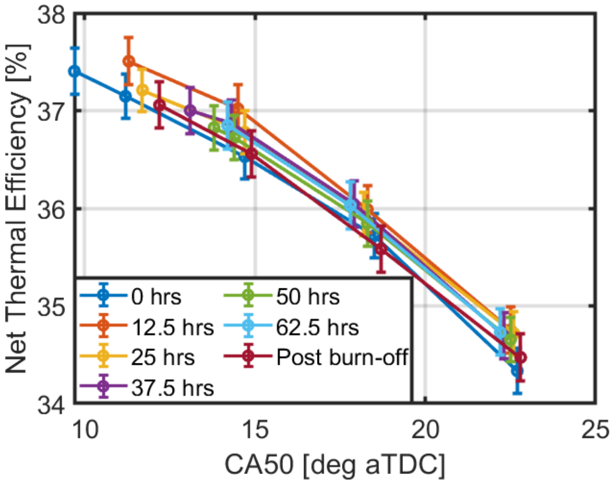

Figure 33: CA50 vs. net thermal efficiency during CCD accumulation (0 hours to 62.5 hours) and CCD burn-off (Post-burn-off).

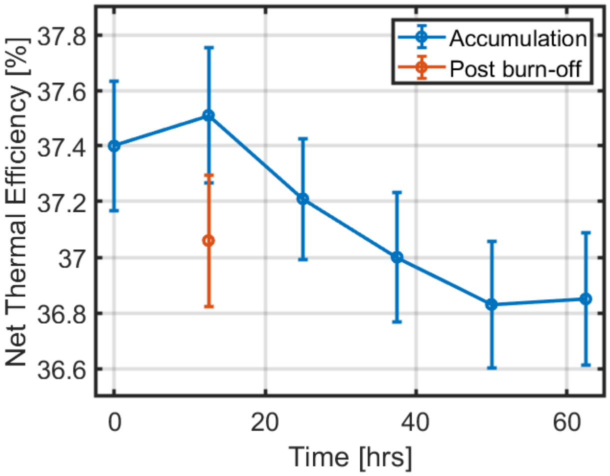

Figure 34: Net thermal efficiency at KLSA during CCD accumulation (0 hours to 62.5 hours) and CCD burn-off (Post-burn-off).

Multiple performance and emissions metrics at a spark timing of -15 degrees aTDC across all sweeps are shown in Table 17. The efficiency gain was consistent across both fuel conversion and thermal efficiency due to the lack of a significant change in combustion efficiency. With constant air and fuel flow rates, the closed cycle load increased, indicating a higher work output through blocked heat transfer. However, the results in Table 17 largely imply that apart from knock and exhaust temperature in Figure 32, the largest changes in performance occurred after 12.5 hours of deposition, and the performance emissions largely remained either unchanged or dithered between the values measured at 0 hours and 12.5 hours. This dithering behavior was also seen in unburned hydrocarbons, which is plotted against CA50 in Figure 35. After the large initial drop at 12.5 hours, continued CCD deposition does no harm or good relative to the 0-hour baseline.

Table 17: Performance and emissions characteristic at a spark timing of -15 degrees aTDC

	Baseline – 0 hours	**12.5 hours**	**25 hours**	**37.5 hours**	**50 hours**	**62.5 hours**	**Post burn-off**
Gross Thermal Efficiency [%]	38.39 ± 0.24	38.98 ± 0.25	38.75 ± 0.23	38.90 ± 0.25	38.80 ± 0.24	38.88 ± 0.25	38.55 ± 0.25

Net Thermal Efficiency [%]	36.53 ± 0.23	37.02 ± 0.24	36.78 ± 0.22	36.88 ± 0.23	36.72 ± 0.23	36.85 ± 0.24	36.56 ± 0.24
Net Fuel Conversion Efficiency [%]	35.07 ± 0.22	35.56 ± 0.23	35.37 ± 0.21	35.39 ± 0.23	35.30 ± 0.22	35.41 ± 0.23	35.14 ± 0.23
Combustion Efficiency [%]	96.52 ± 0.14	96.59 ± 0.17	96.69 ± 0.14	96.49 ± 0.14	96.66 ± 0.13	96.61 ± 0.15	96.64 ± 0.16
CA50 [deg aTDC]	14.70 ± 0.10	14.50 ± 0.15	14.70 ± 0.10	14.30 ± 0.15	14.40 ± 0.15	14.20 ± 0.15	14.90 ± 0.15
is uHC [g/kWhr]	4.36 ± 0.58	3.99 ± 0.25	4.07 ± 0.25	4.21 ± 0.25	4.18 ± 0.25	4.09 ± 0.25	4.11 ± 0.26
is CO [g/kWhr]	12.84 ± 1.45	13.16 ± 0.75	11.88 ± 1.06	13.31 ± 1.38	12.05 ± 1.10	12.63 ± 1.22	12.64 ± 0.90
is NOx [g/kWhr]	16.27 ± 0.23	15.20 ± 0.17	16.42 ± 0.18	16.27 ± 0.16	17.06 ± 0.17	16.53 ± 0.20	16.35 ± 0.23
IMEPg [bar]	7.85 ± 0.03	7.94 ± 0.03	7.92 ± 0.03	7.95 ± 0.03	7.94 ± 0.03	7.96 ± 0.03	7.91 ± 0.03

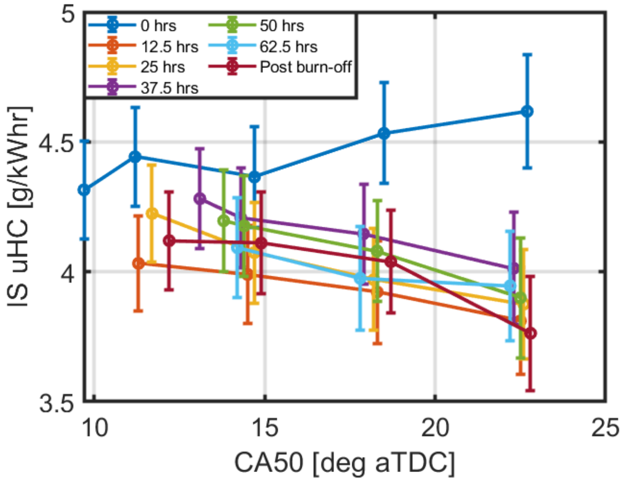

Figure 35: CA50 vs. indicated specific unburned hydrocarbons (is uHC) during CCD accumulation (0 hours to 62.5 hours) and CCD burn-off (Post-burn-off).

Although there was a heat transfer reduction at 12.5-hours relative to the baseline, there did not appear to be a consistent decline in heat transfer losses during the rest of the CCD accumulation phase. A consistent increase in heat transfer losses caused by the high surface roughness of the CCD layer could explain the dithering in net thermal efficiency in Figure 33 and Figure 34. A MetroPro OMP-0347 optical profilometer was available to quantify the roughness of the piston through non-contact means, thus preserving the structural integrity of the CCD layer. In principle, the device uses light to reconstruct the surface topography of the substrate [72]. Roughness average (RA) values for a single point on the clean and CCD covered piston are reported as 0.718 and 1.901 microns, respectively. The baseline TBC was smooth since the surface was polished. It should be noted that the roughness measurement with the optical profilometer was performed on the intake side where less CCDs accumulated. Instrument limits prevented measurements on the exhaust side, where large-scale roughness was visually significant. The raw photos of the surfaces via optical profilometer are provided in Figure 36.

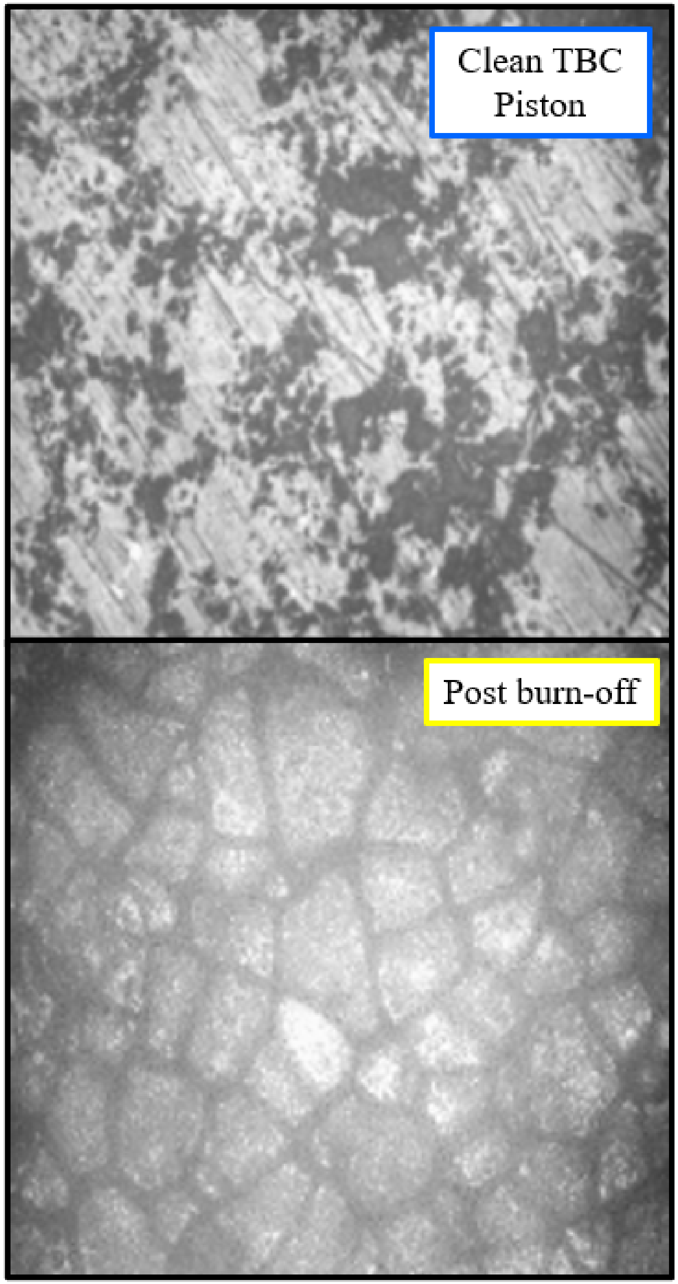

Figure 36: Zoomed in photographs of the clean TBC piston and CCD covered piston after the burn-off phase.

5.5 Discussion: Connecting Properties and Performance

External property measurements with the coated heat flux probe showed that the thermophysical properties of the TBC/CCD system improved. Performance results showed an increase in efficiency and exhaust temperature with a retarded KLSA, consistent with the behavior of a coating system with improved thermophysical properties. The net thermal efficiency at the 12.5-hour mark increased by 0.11 ± 0.47% over the baseline efficiency. Beyond 12.5-hours of CCD growth, the required spark timing retard to achieve an equal knock intensity level further diminished the net thermal efficiency such that no spark timing sweep improved the KLSA efficiency over the baseline. This fact demonstrates that accumulating too much CCD is detrimental to performance, despite the absolute improvement in the thermophysical properties of the coating system. It should be noted that the goal of this study was to accumulate a significant amount of CCDs on the surface of the piston to generate clear performance trends. Results with hundreds of microns of CCDs on some locations of the piston are no representative of true CCD growth on production engines. In a production setting, the driving style would dictate the amount of CCDs that accumulate, along with the fuel properties. The goal of this section was not to explore the effects of various gasoline blends on CCDs and therefore, choosing EPA certification gasoline was a logical decision. However, it does introduce some uncertainty related to how the CCDs would have accumulate, and even what their properties would have been, with other gasoline blends.

CHAPTER 6: CONCLUSIONS

TBCs in spark ignition engines face a variety of challenges due to the knock limitations of the architecture. This thesis demonstrates that low thermal inertia TBCs, characterized by a dynamic temperature swing that allows the surface temperature of the coating to decrease during the intake stroke and prevent charge heating, can enable an efficiency increase. Rather than targeting a direct heat transfer reduction, thin low thermal inertia coatings can enable charge cooling in which the intake air temperature is reduced, countering the knock onset effect of reduced heat transfer during the closed cycle and enabling spark advance. Multiple coating thicknesses, materials, and components were tested in a single-cylinder research engine to determine the best combination of coatings for spark ignition engines. The following conclusions can be drawn from the experiments:

1. A novel low thermal inertia material (called NC) was found to be effective at a thickness close to its penetrative depth. The thinnest coating (120-micron NC piston) produced the largest efficiency gain across all operating conditions compared to the other coated pistons with a maximum net thermal efficiency gain of 0.30% ± 0.44%. This efficiency gain was a result of blocking heat transfer during the closed cycle and charge cooling during the open cycle, allowing the KLSA to advance further than the metal baseline.
2. Thicknesses beyond the material's penetrative depth showed a degradation in efficiency and required a KLSA retard to counteract severe knock.
3. A low thermal inertia with a catalytically active topcoat produced no significant change in emissions, but the improved thermophysical properties of the topcoat allowed the piston to achieve match the knock behavior of the metal baseline compared to the same thickness piston with no topcoat.

4. A piston with gadolinium zirconate coating recorded a maximum absolute net thermal efficiency gain of 0.16% ± 0.42%. This was accompanied by no significant knock penalty, thus demonstrating its potential as a temperature swing coating in a spark ignition engine.
5. A reduction in unburned hydrocarbon and particulate matter emissions were recorded during simulated cold-starts with coated pistons that generated a charge heating penalty during steady-state testing.
6. Applying a coating on the combustion face, backside, and stem of the intake and exhaust valves with the 120-micron NC piston produced the largest average net thermal efficiency benefit across all coating configurations, indicating that increasing the coated surface area is beneficial for efficiency. A slight knock penalty of ~0.5 degrees in spark timing was incurred relative to the metal baseline. Considering that the coated piston by itself generated a spark advance, the efficiency increase was generated through heat transfer reduction rather than producing more favorable combustion phasing.
7. A staged removal of the coated valves showed that the coated exhaust valve generated a significant knock penalty that caused a KLSA retard. The coated intake valve by itself (with the coated piston) generally matched the KLSA of the fully coated configuration, indicating that the coated intake valves alleviated knock.
8. The coated exhaust valve produced the highest exhaust temperatures across all coating configurations, implying that the coated exhaust valve was retaining excess heat.
9. A coated heat flux probe was installed in the single cylinder engine to accumulate CCD for external property measurements. Approximately 30-microns of CCD were accumulated on the surface of the coated heat flux probe.

10. The first 20-microns of CCD growth on the coated heat flux probe showed no clear trend in diffusivity, but further CCD growth showed a slight decline. The conductivity decreased as CCD was accumulated.
11. CCD conductivity was calculated using a thermal resistance network, with the average value falling within the range of previously reported values.
12. Spark timing sweeps every 12.5 hours during the CCD accumulation phase showed a slight increase in net thermal efficiency after 12.5-hours, but declined or remained constant throughout the remainder of the 62.5-hour accumulation period. It was speculated that this constant efficiency after 12.5-hours was due to the roughness of the CCD top-layer, which increased the surface roughness and has been reported in the literature to contribute to higher heat transfer losses. Optical profilometer measurements of the piston confirmed that the roughness increased with CCDs.

REFERENCES

[1] Conway, G., Joshi, A., Leach, L., García, A., Senecal, P. “A review of current and future powertrain technologies and trends in 2020,” *Transportation Engineering*, 5, 100080, 2021, https://doi.org/10.1016/j.treng.2021.100080

[2] Hawkins, T.R., Singh, B., Majeau-Bettez, G., Strømman, A.H., “Comparative Environmental Life Cycle Assessment of Conventional and Electric Vehicles,” *Journal of Industrial Ecology*, 17:158-160, 2013, https://doi.org/10.1111/j.1530-9290.2012.00532.x

[3] U.S. Energy Information Administration, U.S. State Profiles and Energy Estimates, 2020, https://www.eia.gov/state/. Accessed February 2023.

[4] Kim, H.C., Ahn, S., Arsenault, R., Chulheung, B., Lee, J., Wallington, T.J., “Cradle-to-Gate Emissions from a Commercial Electric Vehicle Li-Ion Batter: A Comparative Analysis,” *Environmental Science & Technology*, 50: 7115-7722, 2016, https://doi.org/10.1021/acs.est.6b00830

[5] Buchal, C., Sinn, H.W., “Decarbonizing mobility: Thoughts on an unresolved challenge,” *The European Physical Journal Plus*, 134, 599, 2019, https://doi.org/10.1140/epjp/i2019-13020-6

[6] Nearler, R., Reichmith, D., Anair, D., *Cleaner Cars from Cradle to Grave: How Electric Cars Beat Gasoline Cars on Lifetime Global Warming Emissions*, Union of Concerned Scientists, 2015. https://www.ucsusa.org/sites/default/files/attach/2015/11/Cleaner-Cars-from-Cradle-to-Grave-full-report.pdf. Accessed February 2023.

[7] Holland, S., Mansur, E., Muller, N., Yates, A., *Environmental Benefits from Driving Electric Vehicles?*, National Bureau of Economic Research, 2015. https://www.nber.org/papers/w21291. Accessed February 2023.

[8] Brennan, J., Barder, T., *Battery Electric Vehicles vs. Internal Combustion Engine Vehicles – A United States-Based Comprehensive Assessment*, Arthur D. Little, 2016. https://www.adlittle.com/en/insights/viewpoints/battery-electric-vehicles-vs-internal-combustion-engine-vehicles. Accessed February 2023.

[9] Burton, T., Powers, S., Burns, C., Conway, G. et al., "A Data-Driven Greenhouse Gas Emission Rate Analysis for Vehicle Comparisons," *SAE International Journal of Electrified Vehicles*, 12(1):91-127, 2023, https://doi.org/10.4271/14-12-01-0006

[10] Heywood, J. B. “Internal Combustion Engine Fundamentals,” (New York, McGraw-Hill, 1988), ISBN0- 07-100499-8.

[11] Bryzik, W. and Kamo, R., "TACOM/Cummins Adiabatic Engine Program," SAE Technical Paper 830314, 1983, https://doi.org/10.4271/830314

[12] Kobayashi, H., Yoshimura, K., Hirayama, T., “A study on dual circuit cooling for higher compression ratio,” SAE Technical Paper 841295, 1984, https://doi.org/10.4271/841294

[13] Wong, V., Bauer, W., Kamo, R., Bryzik, W. et al., "Assessment of Thin Thermal Barrier Coatings for I.C. Engines," SAE Technical Paper 950980, 1995, https://doi.org/10.4271/950980.

[14] Assanis, D. and Mathur, T., "The Effect of Thin Ceramic Coatings on Spark-Ignition Engine Performance," SAE Technical Paper 900903, 1990, https://doi.org/10.4271/900903

[15] Marr, M.A., Wallace, J.S., Pershin, L., Chandra, S., Mostaghimi, J., "Preliminary testing of metal-based thermal barrier coating in a spark-ignition engine," *ASME Journal of Engineering for Gas Turbines and Power,* 132(7), 2010, https://doi.org/10.1115/1.4000298

[16] Marr, M., Wallace, J., Memme, S., Chandra, S. et al., "An Investigation of Metal and Ceramic Thermal Barrier Coatings in a Spark-Ignition Engine," *SAE International Journal of Engines*, 3(2):115-125, 2010, https://doi.org/10.4271/2010-01-2090

[17] Poola, R., Nagalingam, B., and Gopalakrishnan, K., "Performance of Thin-Ceramic-Coated Combustion Chamber with Gasoline and Methanol as Fuels in a Two-Stroke SI Engine," SAE Technical Paper 941911, 1994, https://doi.org/10.4271/941911

[18] Yan, Z., Gainey, B., Lawler, B., "A parametric modeling study of thermal barrier coatings in low-temperature combustion engines," *Applied Thermal Engineering*, 200: 117687, 2022, https://doi.org/10.1016/j.applthermaleng.2021.117687

[19] Kosaka, H., Wakisaka, Y., Nomura, Y., Hotta, Y. et al., "Concept of "Temperature Swing Heat Insulation" in Combustion Chamber Walls, and Appropriate Thermo-Physical Properties for Heat Insulation Coat," *SAE International Journal of Engines*, 6(1):142-149, 2013, https://doi.org/10.4271/2013-01-0274

[20] Powell, T., Killingsworth, N., Hoffman, M., O'Donnell, R., Prucka, R., Filipi, Z., "Predicting the gas-wall boundary conditions in a thermal barrier coated low temperature combustion engine using sub-coating temperature measurements," *International Journal of Powertrains*, 6(2):125-150, 2017, https://doi.org/10.1504/IJPT.2017.085679

[21] Powell, T., O'Donnell, R., Hoffman, M., Filipi, Z., "Impact of a Yttria-Stabilized Zirconia Thermal Barrier Coating on HCCI Engine Combustion, Emissions, and Efficiency," *ASME Journal of Engineering for Gas Turbines and Power*, 139(11), 111504, 2017, https://doi.org/10.1115/1.4036577

[22] Powell, T., O'Donnell, R., Hoffman, M., Filipi, Z., Jordan, E.H., Kumar, R., Killingsworth, N., "Experimental investigation of the relationship between thermal barrier coating structured porosity and homogeneous charge compression ignition engine combustion," *International Journal of Engine Research*, 22:88-108, https://doi.org/10.1177/1468087419843752

[23] Chérel, J., Zaccardi, J.M., Bouteiller, B., Allimant, A., "Experimental assessment of new insulation coatings for lean burn spark-ignited engines," *Oil & Gas Science and Technology Rev IFP Energies Nouvelles*, 75(11), 2020, https://doi.org/10.2516/ogst/2020006

[24] Woschni, G., Spindler, W., Kolesa, K., “Heat insulation of combustion chamber walls: a measure to decrease the fuel consumption of I.C. Engines?,” SAE Technical Paper 870339, 1987, https://doi.org/10.4271/870339

[25] Andrie, M., Kokjohn, S., Paliwal, S., Kamo, L. et al., "Low Heat Capacitance Thermal Barrier Coatings for Internal Combustion Engines," SAE Technical Paper 2019-01-0228, 2019, https://doi.org/10.4271/2019-01-0228

[26] Price, R., Wilkinson, J., Jones, D., Morley, C., “A Laboratory Simulation and Mechanism for the Fuel Dependence of SI Combustion Chamber Deposit Formation” SAE Technical Paper 952445, 1995, https://doi.org/10.4271/952445.

[27] Edwards, J., Choate, P., “Average Molecular Structure of Gasoline Engine Combustion Chamber Deposits Obtained by Solid-State ^{13}C, ^{31}P, and ^{1}H Nuclear Magnetic Resonance Spectroscopy”. SAE Technical Paper 932811, 1993, https://doi.org/10.4271/932811.

[28] Cheng, S., "The Impacts of Engine Operating Conditions and Fuel Compositions on the Formation of Combustion Chamber Deposits," SAE Technical Paper 2000-01-2025, 2000, https://doi.org/10.4271/2000-01-2025.

[29] Uehara, T., Takei, Y., Hoshi, H., Shiratani, K., Okada, M., Esaki, Y., “Study on Combustion Chamber Deposit Formation Mechanism-Influence of Fuel Components and Gasoline Detergents,” SAE Technical Paper 971722, 1997, https://doi.org/10.4271/971722.

[30] Noma, K., Noda, T., Isomura, H., Ashida, T. et al., "A Study of Injector Deposits, Combustion Chamber Deposits (CCD) and Intake Valve Deposits (IVD) in Direct Injection Spark Ignition (DISI) Engines II," SAE Technical Paper 2003-01-3162, 2003, https://doi.org/10.4271/2003-01-3162.

[31] Lacey, J., Kameshwaran, K., Filipi, Z., Fuentes-Afflick, P., Cannella, W., “The effect of fuel composition and additive packages on deposit properties and homogeneous charge compression ignition combustion.” *International Journal of Engine Research*, 19(4): 1631-1646. doi:10.1177/1468087419828624

[32] Cheng, S., "A Physical Mechanism for Deposit Formation in a Combustion Chamber," SAE Technical Paper 941892, 1994, https://doi.org/10.4271/941892

[33] Lepperhoff, G., Houben, M., "Mechanisms of Deposit Formation in Internal Combustion Engines and Heat Exchangers," SAE Technical Paper 931032, 1993, https://doi.org/10.4271/931032

[34] Güralp, O., Hoffman, M., Assanis, D., Filipi, Z., Kuo, T.W., Najt, P., Rask, R., "Characterizing the Effect of Combustion Chamber Deposits on a Gasoline HCCI Engine," SAE Technical Paper 2006-01-3277, 2006, https://doi.org/10.4271/2006-01-3277.

[35] Kalghatgi, G., McDonald, C., Hopwood, A., "An Experimental Study of Combustion Chamber Deposits and Their Effects in a Spark-Ignition Engine," SAE Technical Paper 950680, 1995, https://doi.org/10.4271/950680.

[36] Barnes, J., Stephenson, T., "Influence of Combustion Chamber Deposits on Vehicle Performance and Tailpipe Emissions," SAE Technical Paper 962027, 1996, https://doi.org/10.4271/962027

[37] Anderson, C., Uyehara, O., Myers, P., "An In Situ Determination of the Thermal Properties of Gombustion-Chamber Deposits," SAE Technical Paper 820071, 1982, https://doi.org/10.4271/820071

[38] Nishiwaki, K., Hafnan, M., "The Determination of Thermal Properties of Engine Combustion Chamber Deposits," SAE Technical Paper 2000-01-1215, 2000, https://doi.org/10.4271/2000-01-1215.

[39] Hayes, T.K., “Thermal properties of combustion chamber deposits and their effect on engine Heat transfer and octane requirement increase,” Ph.D. thesis, Mechanical Engineering Department, University of Illinois at Urbana-Champaign, 1991.

[40] McBride, B., Zehe, M., Gordon, S., “NASA Glenn Coefficients for Calculating Thermodynamic Properties of Individual Species,” NASA/TP—2002-211556, 2002.

[41] Galloni, E., “Dynamic knock detection and quantification in a spark ignition engine by means of a pressure based method,” *Energy Conversion and Management*, 64: 256-262, 2012, https://doi.org/10.1016/j.enconman.2012.05.015.

[42] Symonds, J.P.R., Reaval, K.S.J., Olfert, J.S., Campbell B.W., Swift J.W., “Diesel soot mass calculation in real-time with a differential mobility spectrometer,” *Journal of Aerosol Science*, 38(1): 52-68, 2007, https://doi.org/10.1016/j.jaerosci.2006.10.001.

[43] Somhorst, J., Uczak De Goes, W., Oevermann, M., Bovo, M., "Experimental Evaluation of Novel Thermal Barrier Coatings in a Single Cylinder Light Duty Diesel Engine," SAE Technical Paper 2019-24-0062, 2019, https://doi.org/10.4271/2019-24-0062

[44] Filipi, Z., Hoffman, M., O’Donnell, R., Powell, T., Jordan, E., Kumar, R., “Enhancing the efficiency benefit of thermal barrier coatings for homogeneous charge compression ignition engines through application of a low-k oxide,” *International Journal of Engine Research*, 22(6): 1906-1923, https://doi.org/10.1177/1468087420918406.

[45] (2002). *Application Specific Probes: The Key to Successful Coating Measurement*, Helmut Fischer GmbH.

[46] Gok, M.G., Goller, G., “State of the Art of Gadolinium Zirconate Based Thermal Barrier Coatings: Design, Processing, and Characterization,” *Methods for Film Synthesis and Coating Procedures*, 2019, https:// doi.org/10.5772/intechopen.85451

[47] Hoffman, M.A., Lawler, B.J., Filipi, Z.S., Güralp, O.A., Najt, P.M., “Development of a Device for the Nondestructive Thermal Diffusivity Determination of Combustion Chamber Deposits and Thin Coatings,” *ASME Journal of Heat and Mass Transfer*, 136(7): 071601, 2014, https://doi.org/10.1115/1.4026908

[48] Hopwood, A., Chynoweth, S., Kalghatgi, G., "A Technique to Measure Thermal Diffusivity and Thickness of Combustion Chamber Deposits In-Situ," SAE Technical Paper 982590, 1998, https://doi.org/10.4271/982590.

[49] Gainey, B., Longtin, J., Lawler, B., "A Guide to Uncertainty Quantification for Experimental Engine Research and Heat Release Analysis," *SAE International Journal of Engines*, 12(5):509-523, 2019, https://doi.org/10.4271/03-12-05-0033.

[50] Uczak de Goes, W., Markocsan, N., Gupta, M., Vaßen, R., Matsushita, K.I., "Thermal barrier coatings with novel architectures for diesel engine applications," *Surface & Coatings Technology*, 396: 125950, 2020, https://doi.org/10.1016/j.surfcoat.2020.125950.

[51] Moughal, K., Samuel, S., "Exhaust Emission Level Reduction in Two-Stroke Engine using In-Cylinder Combustion Control," SAE Technical Paper 2007-01-1085, 2007, https://doi.org/10.4271/2007-01-1085.

[52] Hu, Z., Ladommatos, N., "In-Cylinder Catalysts - A Novel Approach to Reduce Hydrocarbon Emissions from Spark-Ignition Engines," SAE Technical Paper 952419, 1995, https://doi.org/10.4271/952419.

[53] Haenel, P., Kleeberg, H., Tomazic, D., Dolan, S., "Investigation Regarding the Influence of a Catalytic Combustion Chamber Coating on Gasoline Combustion Characteristics, Emission Formation and Engine Efficiency," SAE Technical Paper 2012-01-1097, 2012, https://doi.org/10.4271/2012-01-1097.

[54] Powell, T., "Impacts of Thermal Barrier Coating Morphology and Catalytic Properties on Low Temperature Combustion Engine In-Cylinder Processes," Ph.D. thesis, Automotive Engineering Department, Clemson University, 2018.

[55] Han, Z., Reitz, R., Yang, J., Anderson, R., "Effects of Injection Timing on Air-Fuel Mixing in a Direct-Injection Spark-Ignition Engine," SAE Technical Paper 970625, 1997, https://doi.org/10.4271/970625

[56] Assanis, D. and Heywood, J., "Development and Use of a Computer Simulation of the Turbocompounded Diesel System for Engine Performance and Component Heat Transfer Studies," SAE Technical Paper 860329, 1986, https://doi.org/10.4271/860329

[57] Gainey, B., Gandolfo, J., Filipi, Z., Lawler, B., "Thermodynamic analysis of heat transfer reduction in spark ignition using thermal barrier coatings," *Proceedings of the Institution of Mechanical Engineers, Part D: Journal of Automobile Engineering*, 2023, https://doi.org/10.1177/09544070231189545

[58] Memme, S., Wallace, J.S., "The Influence of Thermal Barrier Coating Surface Roughness on Spark-Ignition Engine Performance and Emissions," *Proceedings of the ASME 2012 Internal Combustion Engine Division Fall Technical Conference*. Vancouver, BC, Canada. September 23-26, 2012. https://doi.org/10.1115/ICEF2012-92078

[59] Andruskiewicz, P., Najt, P., Durrett, R., Biesboer, S., Schaedler, T., Payri, R., “Analysis of the effects of wall temperature swing on reciprocating internal combustion engine processes,” *International Journal of Engine Research*, 19(4): 461–473. https://doi.org/10.1177/1468087417717903

[60] Assanis, D., Wiese, K., Schwarz, E., Bryzik, W., "The Effects of Ceramic Coatings on Diesel Engine Performance and Exhaust Emissions," SAE Technical Paper 910460, 1991, https://doi.org/10.4271/910460.

[61] Nemmar, A., Hoet, P.H.M., Vanquickenborne, B., Dinsdale, D. et al., “Passage of Inhaled Particles Into the Blood Circulation in Humans,” *Circulation*, 105(4):411-414, 2020. https://doi.org/10.1161/hc0402.104118

[62] Kayes, D., Hochgreb, S., “Mechanisms of Particulate Matter Formation in Spark-Ignition Engines. 1. Effect of Engine Operating Conditions,” *Environmental Science & Technology*, 33(22), 3957-3967, 1999, https://doi.org/10.1021/es9810991.

[63] Kayes, D., Hochgreb, S., “Mechanisms of Particulate Matter Formation in Spark-Ignition Engines. 2. Effect of Fuel, Oil, and Catalyst Parameters,” *Environmental Science & Technology*, 33(22), 3968-3977, 1999, https://doi.org/10.1021/es981100w

[64] Kayes, D., Hochgreb, S., “Mechanisms of Particulate Matter Formation in Spark-Ignition Engines. 3. Model of PM Formation,” *Environmental Science & Technology*, 33(22), 3978-3992, 1999, https://doi.org/10.1021/es981101o

[65] Su, J., Lin, W., Sterniak, J., Xu, M., Bohac, S.V., “Particulate Matter Emission Comparison of Spark Ignition Direct Injection (SIDI) and Port Fuel Injection (PFI) Operation of a Boosted Gasoline Engine,” *ASME Journal of Engineering for Gas Turbines and Power*, 136(9): 091513, 2014, https://doi.org/10.1115/1.4027274

[66] Cerit, M., Ayhan, V., Parlak, A., Yasar, H., “Thermal Analysis of a partially ceramic coated piston: Effect on cold start HC emission in a spark ignition engine,” *Applied Thermal Engineering*, 31(2-3): 336-341, 2011, https://doi.org/10.1016/j.applthermaleng.2010.09.015.

[67] Robert, A., Richard, S., Colin, O., Martinez, L., De Francqueville, L., “LES prediction and analysis of knock combustion in a spark ignition engine,” *Proceedings of the Combustion Institute*, 35(3): 2941-2948, 2015, https://doi.org/10.1016/j.proci.2014.05.154

[68] Merola, S.S., Vaglieco, B.M., “Knock investigation by flame and radical species detection in spark ignition engine for different fuels,” *Energy Conversion and Management*, 48(11): 2987-2910, 2007, https://doi.org/10.1016/j.enconman.2007.07.011.

[69] Hoffman, M.A., Lawler, B.J., Güralp, O.A., Najt, P.M., Filipi, Z.S., “The impact of a magnesium zirconate thermal barrier coating on homogeneous charge compression ignition operational variability and the formation of combustion chamber deposits,” *International Journal of Engine Research*, 16(8): 968-981, 2015, https://doi.org/10.1177/1468087414561274.

[70] Casalegno, V., Vavassori, P., Valle, M., Ferraris, M., Salvo, M., Pintsuk, G., “Measurement of thermal properties of a ceramic/metal joint by laser flash method,” *Journal of Nuclear Materials*, 407(2): 83-87, 2010, https://doi.org/10.1016/j.jnucmat.2010.09.032.

[71] Hoffman, M.A., “Characterization of Combustion Chamber Deposits Formed During Homogeneous Charge Compression Ignition and the impact of a Thermal Barrier Coating on Deposit Accumulation and HCCI Operability,” Ph.D. thesis, Mechanical Engineering Department, University of Michigan, 2012.

[72] Li, Q., Gao, H., Xue, S., “Optical profilometer based on the principle of differential interference,” *Optical Engineering*, 40(5): 833-836, 2001, https://doi.org/10.1117/1.1359794.

APPENDIX A

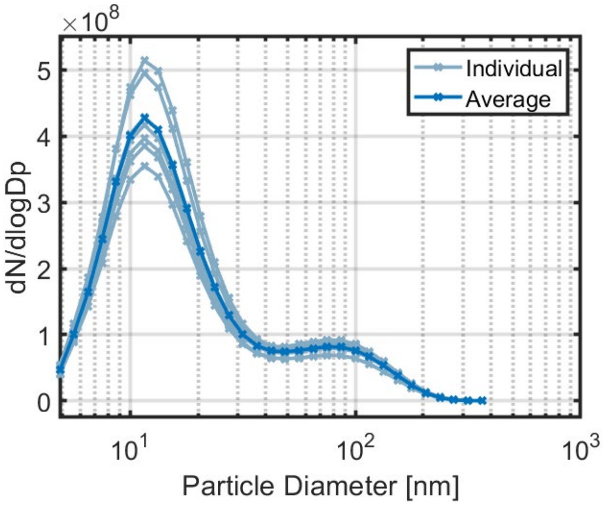

Figure 37: Particle count distribution vs. particle diameter of eight individual cold-start tests using the metal baseline piston.

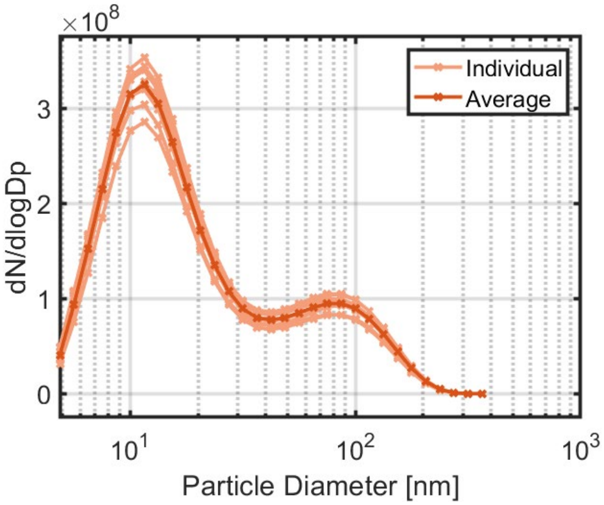

Figure 38: Particle count distribution vs. particle diameter of eight individual cold-start tests using the 120-micron NC piston.

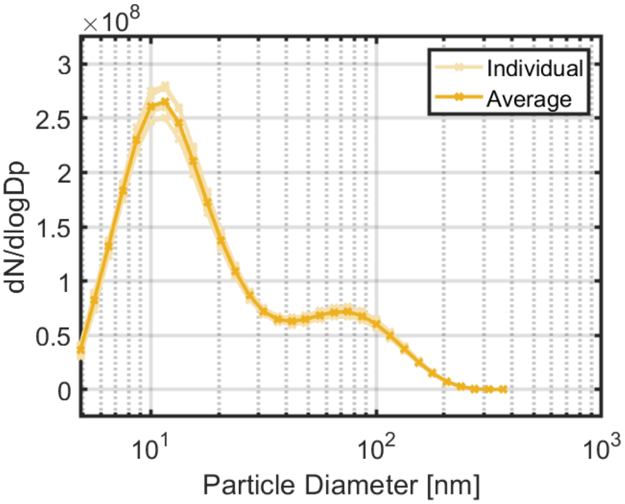

Figure 39: Particle count distribution vs. particle diameter of eight individual cold-start tests using the 200-micron NC piston.

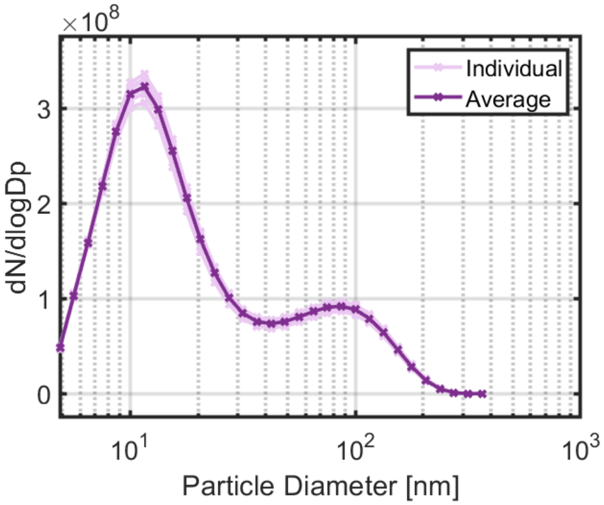

Figure 40: Particle count distribution vs. particle diameter of eight individual cold-start tests using the 200-micron NC w/ CCC piston.

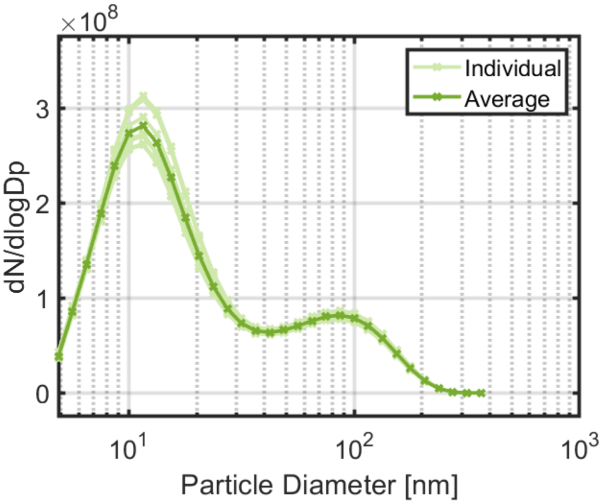

Figure 41: Particle count distribution vs. particle diameter of eight individual cold-start tests using the 200-micron GZO piston.

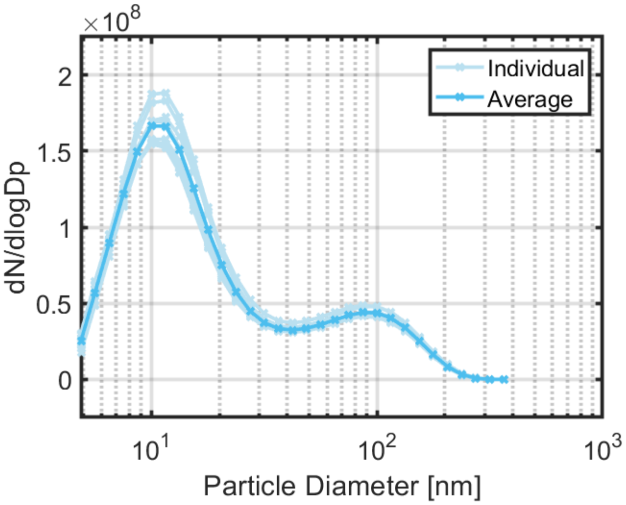

Figure 42: Particle count distribution vs. particle diameter of eight individual cold-start tests using the 375-micron NC piston.

APPENDIX B

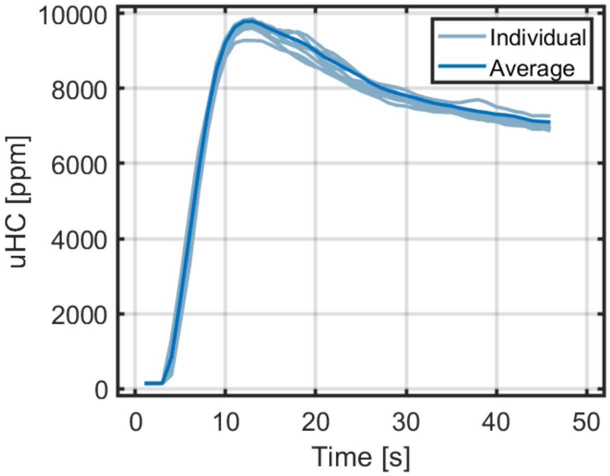

Figure 43: Unburned hydrocarbon emissions (uHC) during the eight individual cold-start tests using the metal baseline piston.

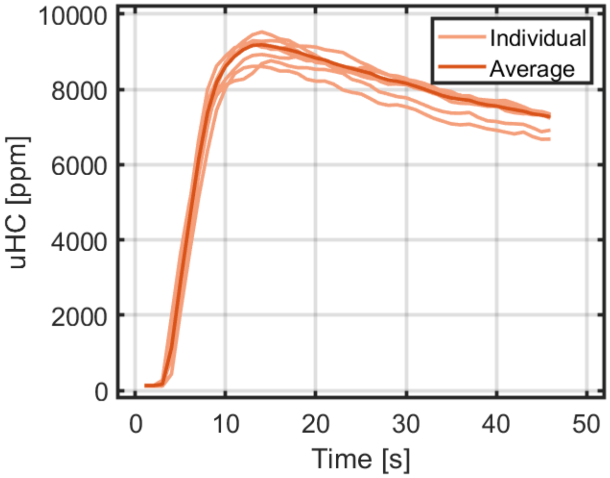

Figure 44: Unburned hydrocarbon emissions (uHC) during the eight individual cold-start tests using the 120-micron NC piston.

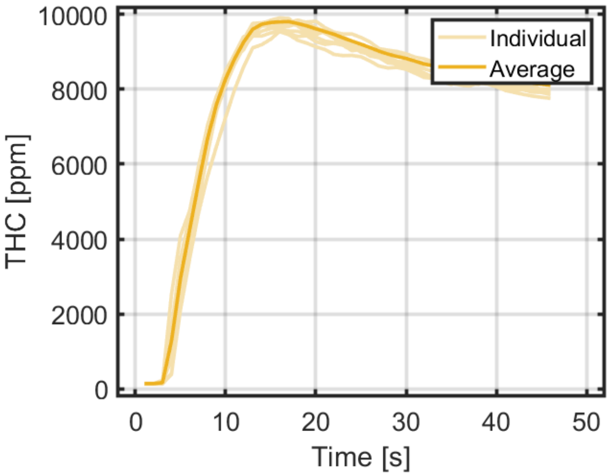

Figure 45: Unburned hydrocarbon emissions (uHC) during the eight individual cold-start tests using the 200-micron NC piston.

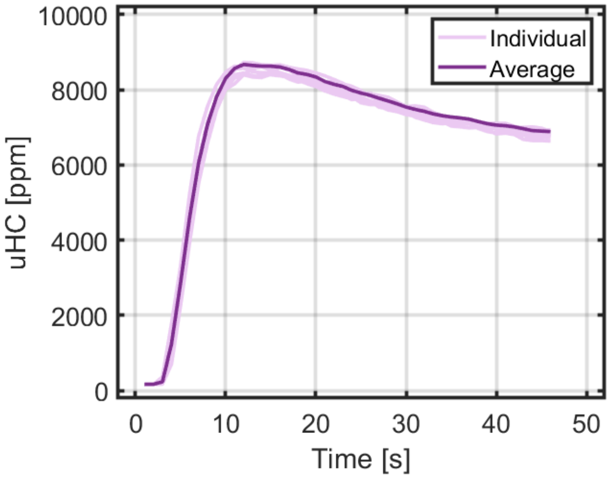

Figure 46: Unburned hydrocarbon emissions (uHC) during the eight individual cold-start tests using the 200-micron NC w/ CCC piston.

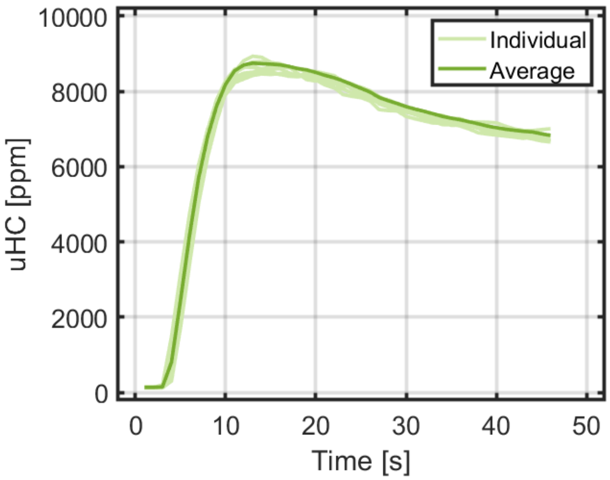

Figure 47: Unburned hydrocarbon emissions (uHC) during the eight individual cold-start tests using the 200-micron GZO piston.

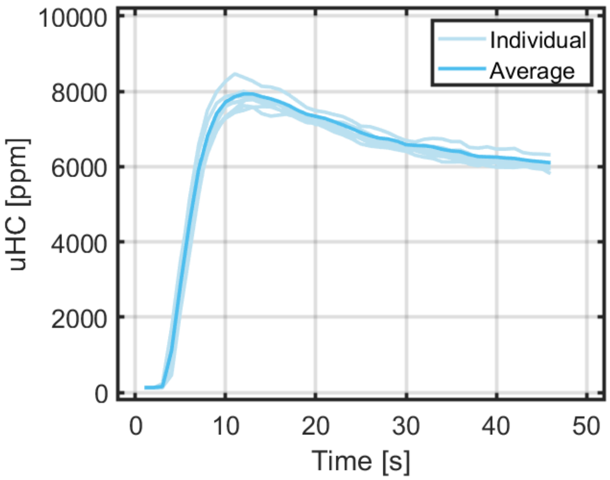

Figure 48: Unburned hydrocarbon emissions (uHC) during the eight individual cold-start tests using the 375-micron NC piston.